RIVISTA DEL NUOVO CIMENTO Vol. 37, N. 9 2014
DOI 10.1393/ncr/i2014-10104-8

X-ray phase contrast imaging: From synchrotrons to conventional sources

A. Olivo(1)(*) and E. Castelli(2)

(1) *UCL Department of Medical Physics and Bioengineering Gower St., London WC1E 6BT, UK*

(2) *Università di Trieste and INFN, Sezione di Trieste Via A. Valerio 2, 34127 Trieste, Italy*

ricevuto il 16 Giugno 2014

Summary. — Phase-based approaches can revolutionize X-ray imaging and remove its main limitation: poor image contrast arising from low attenuation differences. They exploit the unit decrement of the real part of the refractive index, typically 1000 times larger than the imaginary part driving attenuation. This increases the contrast of all details, and enables the detection of features classically considered "X-ray invisible". Following pioneering experiments dating back to the mid-sixties, X-ray phase contrast imaging "exploded" in the mid-nineties, when third generation synchrotron sources became more widely available. Applications were proposed in fields as diverse as material science, palaeontology, biology, food science, cultural heritage preservation, and many others. Among these applications, medicine has been constantly considered the most important; among medical applications, mammography is arguably the one that attracted most attention. Applications to mammography were pioneered by the SYRMEP (SYnchrotron Radiation for MEdical Physics) group in Trieste, which was already active in the area through a combination of innovative ways to do imaging at synchrotrons and development of novel X-ray detectors. This pioneering phase led to the only clinical experience of phase contrast mammography on human patients, and spawned a number of ideas as to how these advances could be translated into clinical practice.

PACS 87.59.-e – X-ray imaging.
PACS 41.60.Ap – Synchrotron radiation.
PACS 87.59.E- – Mammography.
PACS 42.25.Gy – Edge and boundary effects; reflection and refraction.

(*) E-mail: a.olivo@ucl.ac.uk

1. – X-ray phase contrast imaging *vs.* conventional X-ray imaging

The idea of using X-rays to produce images of the inner parts of the body dates back to the discovery of X-rays themselves: Röntgen's radiograph of his wife's hand was taken only a month and a half after he discovered X-rays [1, 2]. To some extent surprisingly, despite very significant innovations like computed tomography [3, 4] and the advent of digital detectors [5], the physical principle exploited to generate image contrast has remained the same since then. This principle is the difference in the X-ray attenuation coefficients of different materials (fig. 1).

This is a simple, straightforward and very effective way to generate image contrast with X-rays. Calculating this contrast is also rather simple. If one defines the attenuation contrast as

$$C_{\mathrm{att}} = \frac{I_1 - I_2}{I_1}\,, \tag{1}$$

where I_2 is the X-ray intensity transmitted in the shadow of the detail and I_1 the intensity transmitted immediately outside it, then using Beer-Lambert's law [6] one obtains

$$I_1 = I_0 \exp(-\mu_1 t_1); \qquad I_2 = I_0 \exp[-\mu_1(t_1 - t_2)] \exp(-\mu_2 t_2), \tag{2}$$

where I_0 is the X-ray intensity incident on the object, μ_2 the attenuation coefficient of the detail, μ_1 the attenuation coefficient of the background, t_2 and t_1 the thicknesses of detail and background, respectively. By inserting the results of eq. (1) into the definition of C_{att}, one obtains [7]

$$C_{\mathrm{att}} = 1 - \exp[(\mu_1 - \mu_2)t_2], \tag{3}$$

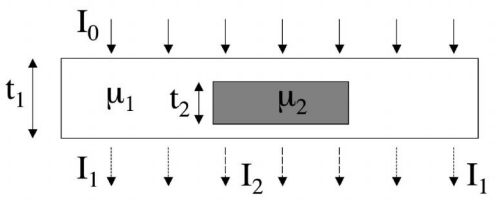

Fig. 1. – Contrast formation in conventional X-ray imaging.

from which it appears immediately obvious that the conventional attenuation contrast tends to vanish if a) $\mu_1 \sim \mu_2$, *i.e.* the difference between the attenuation coefficients of detail and background is small, or if b) $t_2 \sim 0$, *i.e.* the detail is thin.

Being based on a different physical principle, X-Ray Phase Contrast imaging (XPCi) can help in both the above cases. The best way to understand the underpinning physical difference is to refer to the complex refractive index n:

$$n = 1 - \delta + i\beta, \tag{4}$$

where i is the imaginary unit. The imaginary term β is linked to the attenuation properties of a given material, and in fact, within reasonable approximation one can write [8]

$$\mu = \frac{4\pi\beta}{\lambda}, \tag{5}$$

where λ is the X-ray wavelength. On the other hand, δ is responsible for the phase shift Φ suffered by the X-ray wave field when it transverses a given thickness of material

$$\Phi(x, y) = \frac{2\pi}{\lambda} \int_{\text{object}} \delta(x, y, z) \mathrm{d}z, \tag{6}$$

where z is the propagation direction of the X-rays, and the integral is extended over the thickness of the imaged object along z. δ is directly linked to the electron density ρ_e of a given material, and to good approximation (*e.g.* away from absorption edges) one can write

$$\delta = \frac{r_e \rho_e \lambda^2}{2\pi}, \tag{7}$$

where r_e is the classical electron radius. Both δ and β are effectively related to the real and imaginary part of the atomic scattering factors, and more detail on this can be found in [9]. They have very different dependences upon X-ray energy (fig. 2), and the noteworthy aspect here is that, for most materials and over the range of energies commonly employed in X-ray imaging, δ is much larger than β —typically up to 1000 times larger. This means that, if properly exploited, phase effects can lead to a dramatic increase in image contrast. However, as will be clearer from the following, this contrast manifests itself in a rather different form compared to C_{att}. Typically, in XPCi single (see sects. **2**˙2, **2**˙4 and **2**˙5) or double (sect. **2**˙3) pairs of dark/bright fringes underline

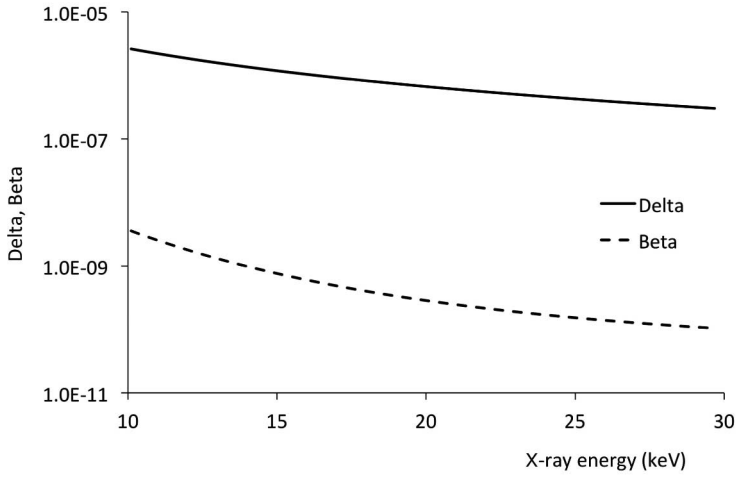

Fig. 2. – Values of δ and β for PMMA (often used as a tissue substitute in phantoms) between 10 and 30 keV. The semi-logarithmic graph shows both the large difference between δ and β values, and their different dependence on X-ray energy.

the presence of details in an image. As a consequence, the (phase) contrast of a given detail is often re-defined as

$$C_{\text{phase}} = \frac{I_{\max} - I_{\min}}{I_{\text{background}}}, \tag{8}$$

where $I_{\max}$ and $I_{\min}$ are the maximum and minimum intensities observed on the bright and dark fringes respectively, while $I_{\text{background}}$ is the intensity observed away from the detail. Only when crystal interferometers (see sect. **2**˙1) are used, which are directly sensitive to phase rather than to its first or second derivative like the methods described in sects. **2**˙2-**2**˙5, definitions of contrast more similar to the standard "area" contrast concept underpinned by eq. (1) can be adopted. Alternatively, these first and second derivatives of the phase term must be integrated to yield a "pure phase" image, which normally comes at the cost of significant image artefacts. These technical aspects will be discussed in more detail in the following sections.

Quite obviously, changes in Φ have been present since the origins of X-ray imaging: the fact that they had never been spotted before dedicated experiments were set up indicates that normally they do not manifest themselves. In fact, since X-ray detectors are sensitive to changes in X-ray intensity, strategies must be devised that enable converting changes in Φ into intensity differences on the detector. Broadly speaking, two main principles are exploited: the detection of interference patterns [10-12], or the use of X-ray refraction [13-15].

Figure 3 shows effectively the same situation as shown in fig. 1, where however the incident X-rays are represented in terms of wave fronts, and the detail and its background have been characterized by means of their δ instead of their μ (*i.e.*, β) values. A detail causing an advanced wave front is represented, which is the situation encountered when $\delta_2 > \delta_1$; if $\delta_1 > \delta_2$, the wave front behind the detail would be delayed. It should be noted, however, that the case of advanced wave front is always encountered for isolated

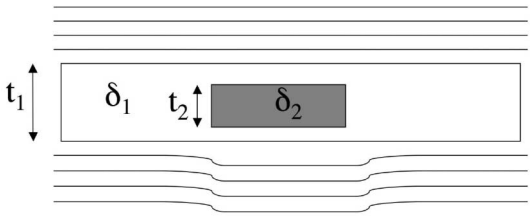

Fig. 3. – Interpretation of X-ray interaction with a sample consisting of a detail immersed in a uniform background in terms of wave effects.

objects (*i.e.* ideally surrounded by vacuum, in practice by air) since, as made clear by eq. (4) jointly with the fact that for X-rays δ is positive (fig. 2), for X-rays the real part of the refractive index is negative (N.B.: this does not of course violate relativity, as the group velocity still does not exceed the speed of light [16]).

Regardless of whether we are dealing with an advanced or delayed wave front, this distortion can be used to generate detectable intensity changes. These are obtained either by letting the wave propagate though a sufficient distance so that perturbed and unperturbed components of the wave front interfere thus generating a detectable pattern [11, 12], or by re-combining the perturbed wave with its unperturbed version in an interferometer [10]. Details on both these approaches are given in the next section.

An alternative approach consists in picking up faint changes in the X-ray propagation direction. This requires remembering that, locally, the direction of the X-ray is orthogonal to the wave front. As a consequence, a local distortion in the wave front translates directly into a small change in the propagation direction. This is schematically represented in fig. 4.

This is effectively X-ray refraction, analogous to refraction in the visible light regime, only involving much smaller angles (typically of the order of the microradian: the angle under which 1 mm is seen from a distance of 1 km). This deviation depends on the local variation in the phase shift, and is maximal where the phase changes most abruptly. In fact, the refraction angle α can be calculated by taking the first derivative of the phase shift Φ (given by eq. (6))

$$\alpha \cong \frac{\lambda}{2\pi} \nabla_{x,y} \Phi, \tag{9}$$

where $\nabla_{x,y}$ indicates the two-dimensional gradient (Φ does not depend on z, as made clear by the integral in eq. (6)), with the two partial derivatives yielding the two components of the refraction angle.

This is a simplified description, that corresponds to reverting from a wave optics to an (approximated) ray-optics representation of the phenomenon. However, as will be discussed in more detail below, this is an effective and reliable description, which holds under a wide and varied range of circumstances [17, 18].

While this introductory section outlined the concepts of attenuation and phase-based contrast, and discussed the general principles on the basis of which phase changes mechanisms can be exploited to generate image contrast, the next chapter will examine in more detail the specific methods that have been developed so far to achieve this in practice.

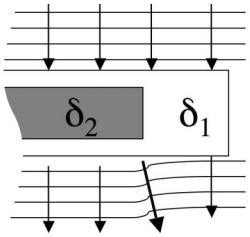

Fig. 4. – How, in the ray-tracing representation, object-induced wave front distortions translate into local changes in the X-ray propagation direction (for ease of visualization, the deviation has been highly exaggerated in the figure).

Section **3** will then discuss the importance of mammography as a "key" application of XPCi, and review the important results obtained in Trieste, in what is to date the only *in vivo* application of XPCi to human patients. Finally, sect. **4** will look into possible options to translate the successful results obtained in Trieste more broadly into clinical settings, which would require eliminating the need for synchrotron sources.

2. – X-ray phase contrast imaging methods

This section will follow an historical perspective, meaning for example that, albeit the "free-space propagation" or "in-line holography" approach hinted at immediately below fig. 3 is effectively simpler, the crystal-based X-ray interferometer will be discussed first, as it was the first XPCi method to be developed and used. For the same reason, refraction-based methods like analyser-based imaging will also be discussed before free-space propagation. The next five sub-sections will discuss the main five XPCi methods following the order with which they were introduced.

2˙1. *Bonse-Hart interferometry.* – The first phase contrast images were obtained making use of the crystal interferometer developed in 1965 by Bonse and Hart [10, 19].

Figure 5 shows a top view of the instrument. All crystal blades operate in Laue mode: the first one (also called "beam splitter" S) splits the incoming beam in two; the second one ("mirror" M) sends (parts of the) separated beams again towards the same direction. The two beams therefore meet again in a position symmetrical to S with respect to M: here, an interference pattern is formed. However, the fringes in this pattern have the same spacing as the Bragg planes in the crystal, and are therefore very difficult to detect directly: the problem is solved by the introduction of the 3rd crystal blade (the "analyser" A). An additional arrangement often used to simplify the imaging process is the introduction of a phase shifter (*e.g.* a wedge-shaped object) in one of the two branches of the interferometer, in a method called *fringe scanning* [20]. The phase shifter creates regularly spaced ("carrier") fringes, and the displacement of these fringes caused by the introduction of a sample can be related back to the phase shift caused by the sample itself.

An important thing to notice is that all three blades S, M and A are attached to a common base, not visible in the top view schematic of fig. 5. In fact, crystal interferometers are normally obtained by channel-cutting a single crystal block, which guarantees that the distances between the blades is correct to within the required (subatomic) distance.

Following an important attempt by Ando and co-workers [21], and although Hart did some significant imaging experiments himself [22], the Bonse-Hart interferometer was

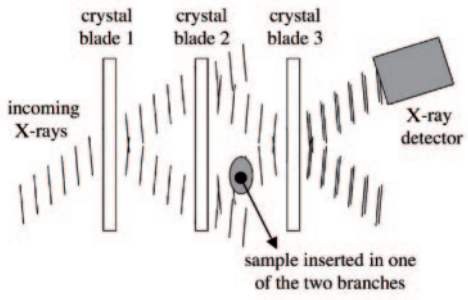

Fig. 5. – Schematic representation of the Bonse-Hart interferometer.

widely used in the mid-nineties by Momose and his group for medical imaging experiments [23-27]. 1995 is the year in which XPCi "exploded": several papers exploiting different approaches were published by various groups (see below), in a sudden significant increase of interest (partially due to 3rd generation synchrotron machines becoming more widely available) that lasts to these days. Among these, Momose's 1995 NIM A [23], with its Jan. 1 publication date, is incontestably the first, and presents preliminary results achieved in 1994 and before (the paper was submitted on March 1, 1994). In the following years, Momose repeatedly showed increased tumour detectability [24], which was also extended to CT approaches [25], and started looking at different tissues such as brain [26] and blood [27].

Although a direct comparison is made difficult by its direct dependence on Φ (while other methods are sensitive to either the first or second derivative of Φ), Bonse/Hart interferometry tends to be considered the most sensitive XPCi method [28], and this is reflected directly by the stunning results obtained on soft biological tissues by Momose and other researchers. However, the method is not of straightforward use, is highly sensitive to vibrations and alignment errors, and most of all offers a limited field of view due to the monolithic nature of the crystal the interferometer is obtained from. For these reasons, its use has decreased since the mid-90 s, and, to the best of our knowledge, no attempt has been made at translations for "mainstream" use with conventional sources. However, creative new flexible and "multi-modal" implementations, often straddling crystal interferometry and the analyser-based methods described in the next section, have been proposed by Ando and his group [29-31].

2˙2. *Analyzer-based imaging.* – A significant simplification of the Bonse/Hart interferometer comes from the use of a single crystal as an "analyser" of sample-induced changes in the X-ray direction, hence the name "analyser-based imaging" (ABI). Although only one crystal (sometimes two, in a "double-bounce" configuration) is used as post-sample beam analyser, more crystals are needed for beam preparation upstream of the sample. In synchrotron experiments, these are typically provided by the beamline monochromator (see fig. 6), while more crystals have to be added to the set-up if a conventional source is used (see *e.g.* fig. 1 in ref. [13]; this is more clearly appreciable in the related patent [32], which also presents some alternative designs).

A possible embodiment at a synchrotron beamline is shown in fig. 6. Note that the beam cross-section is typically small (a few mm) at least in one direction —normally the vertical one— while it can be sufficiently large as to cover the entire sample in the

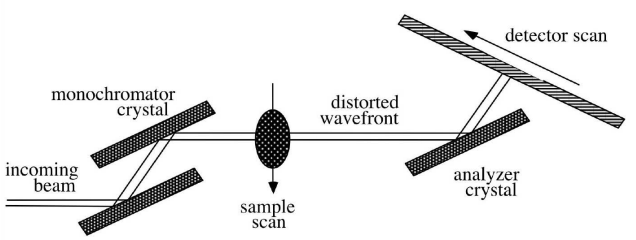

Fig. 6. – Analyzer-based imaging in its synchrotron implementation. The X-ray beam, coming from the left-hand side, is monochromatized by a double-bounce crystal, traverses the sample, is further reflected by the "analyser" crystal and eventually reaches the detector.

horizontal one (*i.e.* the direction entering the plane of the drawing in fig. 6). As a consequence, two-dimensional images are obtained by scanning the sample through this "laminar" beam. This could be coupled either with a linear detector (which is read out at every sample position, the stored image rows then being recombined to form the full 2D image) or, if an area detector is used, this also has to be scanned through the beam. If a single analyser crystal is used as in fig. 6, not only must the detector plane have an inclination which depends on the crystal's Bragg angle (and therefore on the beam energy): sample and detector must also be scanned in opposite directions, to compensate for the inversion caused by the crystal's reflection (see how the bottom part of the beam becomes the top part after the analyser crystal, and vice versa). Both detector inclination and need to scan in opposite directions are avoided if a double-bounce analyser crystal is used.

In both cases, the analyser crystal's narrow reflectivity curve [33] is exploited to generate image contrast arising from refraction, as schematized in fig. 7. Effectively, rather than the intrinsic reflectivity curve, the "rocking" curve —*i.e.* the variation in intensity observed while rotating the crystal around the axis entering the plane of the drawing in figs. 6 and 7, is used. This is a smoother, bell-shaped function that results from the convolution of the intrinsic reflectivity curves of analyser and monochromator

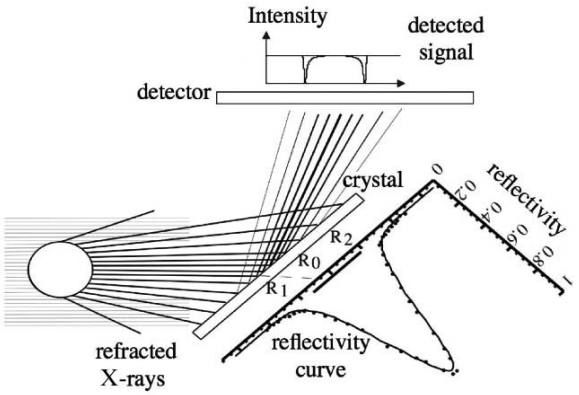

Fig. 7. – Image formation principle in analyser-based imaging.

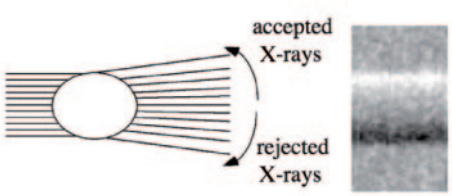

Fig. 8. – Imaging on the 50% slope of the rocking curve.

crystals, plus the contribution from the beam divergence [34]. At a fixed monochromatic energy, as is to a good approximation the case here, thanks to the monochromator crystal upstream of the sample, this curve determines the probability with which X-rays are redirected towards the detector by the analyser crystal. In the situation represented in fig. 7, the analyser crystal is positioned at the top of the reflectivity for the primary beam, *i.e.* at the Bragg angle. The sample causes X-rays to refract, on the basis of the expression given in eq. (9) —angles are highly exaggerated in fig. 7 for simplicity's sake. If, for example, one inserts a homogeneous sphere, or a cylindrical fibre with its axis orthogonal to the plane of the drawing, this acts like a diverging lens in the X-ray regime (due to the real part of the refractive index being smaller than unity, see eqs. (4) and (7)), with X-rays hitting the edges of the sample being refracted at the highest angles, as there the gradient of the phase change is maximum. If the refraction angle is larger than half the full width at half-maximum (FWHM) of the rocking curve, then these deviated X-rays have a small probability of being re-directed by the crystal towards the detector. Areas of diminished intensity, as represented in the intensity plot at the top of fig. 7, are therefore created in correspondence to these sample positions: *e.g.*, if the sample were a fibre entering the plane of the drawing, these would be visible as fringes of reduced intensity running along both edges of the fibre. Image contrast is thus being created that originates from refraction, *i.e.* that depends on δ and not on β.

The system's sensitivity to this type of contrast can be enhanced by using a different orientation of the crystal, *e.g.* by rocking it off its Bragg position by half the FWHM of the rocking curve. This corresponds to 50% reflectivity for primary, unrefracted X-rays, and has the significant advantage that we are now in the position where the slope of the rocking curve assumes maximum steepness. This means that a small change in the direction with which the X-ray hits the crystal surface (*i.e.* effectively the refraction angle) translates into a large difference in the crystal reflectivity, *i.e.* in the chance that X-ray has to be or not be re-directed towards the detector.

A graphical representation is given in fig. 8, where the change in X-ray direction is schematized on the left-hand side, and the corresponding image of a fibre entering the plane of the drawing is shown on the right-hand side. Photons traversing the sample roughly at the centre suffer very little or no deviation. Consequently, they are re-directed towards the detector with 50% efficiency, just like X-rays not hitting the sample at all. In fact, the grey level inside and outside the sample shown in fig. 8 is the same: a "phase" object, *i.e.* an object presenting negligible X-ray absorption, was deliberately chosen in this case, and refraction is thus to a good approximation the only source of contrast. However, the situation is very different for X-rays hitting opposite edges of the sample. These are refracted in opposite directions: hence, those hitting one edge are sent towards

the top of the rocking curve (in this case, the ones deviated upwards, *i.e.* those hitting the top edge of the sample). This corresponds to a much higher reflection probability: more photons are therefore redirected towards the detector, and a positive (bright) fringe is created. The opposite occurs for X-rays refracted in the opposite direction, *i.e.* in this case downwards: these will be sent towards a region of the rocking curve with very low reflectivity, much lower than the 50% reflectivity of unrefracted photons —therefore a negative (dark) fringe will be created. It should be noted that, by changing the direction along which the crystal is rocked off the Bragg position, positive and negative fringes are inverted: this corresponds to switching the phase contrast signal, while absorption, if present, would remain the same. In fact, a few years after the method was introduced, this effect was exploited by Chapman and co-workers to develop one of the first methods to separate phase and absorption ("phase retrieval"), by taking two images on opposite slopes of the rocking curve and alternately eliminating phase and absorption components through an opportunely weighted sum/subtraction [35]. Chapman called this approach "Diffraction Enhanced Imaging" (DEI), and the name became so popular that for a few years it was used interchangeably with ABI to indicate the imaging method itself, as well as the phase retrieval algorithm.

The direct link between image contrast and refraction angle, and therefore its dependence on the first derivative of the phase shift (eq. (9)), makes ABI the first "differential" phase contrast imaging method, a characteristic it now shares with edge illumination and grating interferometry (see below).

Generally speaking, ABI became very popular in the mid-nineties, especially thanks to the famous 1995 Nature letter by Wilkins' group [13], and still remains a widely used technique to this day. It has to be said, however, that a few little known examples exist that pre-date that deservedly famous paper, where effectively the same method had been used to address specific scientific problems, and the results were published in journals with relatively limited diffusion [36,37]. In general, it looks like most ABI-related research pre-dating Wilkins *et al.*'s letter was conducted in the former Soviet Union (see, *e.g.*, [37]), and published in Russian journals which at the time found limited (if any) diffusion in the Western World. Wilkins himself, in the patent [32] immediately preceding his *Nature* letter, quotes a patent by a Russian group [38], which was published internationally in 1992, but was of course preceded by a Russian patent application. Indeed, shortly after the publication of Wilkin's letter and still in 1995, two of the inventors on that patent (Ingal and Beliaevskaya) published an article in an internationally renowned journal of applied physics, which went on to become another highly cited, landmark paper on the subject [14].

Following planar implementations, CT implementations were explored first by Dilmanian [39], then perfected by many others (see, *e.g.* [40-43]). Several parameters assume a particular importance when ABI is combined with CT (*e.g.* the relative orientations of the axis of CT rotation and the one around which the crystal is rocked); however, a detailed discussion of CT implementations lies beyond the scope of the present review paper, and the reader is referred to the quoted papers (and references therein) for details.

Another key development that was achieved through ABI, typically involving further developments of Chapman's original DEI algorithm, is "dark field" or "ultra-small angle scatter" imaging. Researchers started to observe that, alongside the local lateral (*i.e.* angular) shift of the rocking curve due to sample-induced refraction, an additional observable effect was a local "broadening" of the curve itself. This was attributed to multiple refraction in different directions caused by structures in the sample too small to be resolved by the detector pixels: in this sense, it is an indication of the "inhomogene-

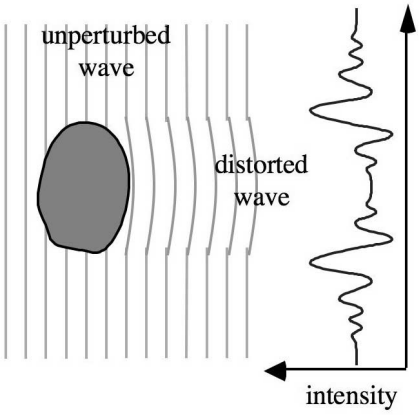

Fig. 9. – "Free-space propagation" or "in-line holography" phase contrast imaging.

ity" of the sample on the sub-pixel scale —*e.g.* a partially crystalline material creates a much stronger "dark field" signal than an amorphous and homogeneous one. Interestingly, three separate groups (at Elettra in Trieste, at the ESRF and in the US) came to the same conclusion, and formulated independent approaches which however have clear common bases [44-46]. Interestingly, this same "broadening" is mentioned by Wilkins in his 1995 patent [32] (but, to the best of our knowledge, not in a published paper): he mentions this not with reference to ABI, despite it being the main subject of the patent, but with reference to an aperture-based implementation of the Shack-Hartmann concept which has more than one point in common with the "edge illumination" method discussed below (sect. **2**˙4).

The "dark field" approach was also translated into CT implementations by Rigon *et al.* first [47], then by Ando's group [48] and others.

The list of medical applications explored with ABI is way too long to be discussed thoroughly here; it includes breast imaging, interestingly since the early days of the method [34,49] as well as in CT [50] and at very low dose [51]; cartilage [52], also *in vivo* on small animals [53]; bone/implant integration [54], lung functionality [55], and much, much more —the authors apologize for all the interesting work that is not quoted here, but providing a full list lies outside the scope of this review.

2˙3. *Free-space propagation or in-line holography.* – In another landmark 1995 paper [11], Snigirev and co-workers demonstrated that, if a source of sufficient coherence is available, phase effects can be observed without the need for any optical element. This extremely simple principle is schematized in fig. 9: by placing the detector at some distance from the sample, rather than directly in contact with it as is normally done in conventional radiology, an interference pattern is generated. If a sufficient propagation distance is introduced, the portion of the wave that has traversed the sample and is, as a consequence, distorted, will interfere with the unperturbed components of the wave front travelling immediately outside the sample itself (which therefore plays the role of the "reference" wave).

The phenomenon can be easily interpreted in terms of near-field Fresnel diffraction [56], as already pointed out by Snigirev in his 1995 paper, and specifically by means

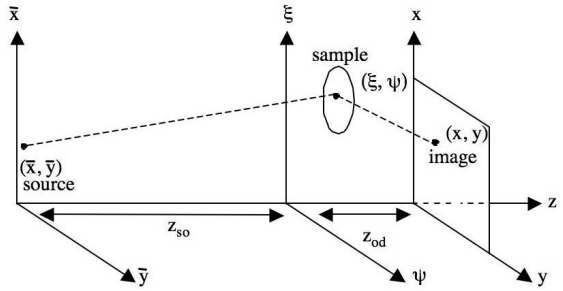

Fig. 10. – Reference frame for the formulation of free-space propagation XPCi in terms of Fresnel/Kirchhoff diffraction integrals.

of the Fresnel/Kirchhoff diffraction integral

$$E(x,y) = -\frac{i\cos\theta}{\lambda}\int \mathrm{d}\xi \int \mathrm{d}\psi f(\xi,\psi), \tag{10}$$

where $E(x,y)$ is the electric field at the generic point x, y of the image plane, and the integral over ξ, ψ extends over the entire sample plane (see fig. 10). θ is the inclination factor [56], and is often assumed to be ~ 0 if the longitudinal distances (z_{so}, source-to-object distance and z_{od}, object-to-detector distance) are much larger than the transverse dimensions of the imaged object, as is practically always the case in synchrotron radiation experiments.

The function f is given by

$$f(\xi,\psi) = \frac{\exp(2\pi i/\lambda\{[z_{\mathrm{so}}^2 + (\overline{x}-\xi)^2 + (\overline{y}-\psi)^2] + [z_{\mathrm{od}}^2 + (\xi-x)^2 + (\psi-y)^2]\}}{\sqrt{[z_{\mathrm{so}}^2 + (\overline{x}-\xi)^2 + (\overline{y}-\psi)^2][z_{\mathrm{od}}^2 + (\xi-x)^2 + (\psi-y)^2]}} \times \exp[i\Phi(\zeta,\psi)], \tag{11}$$

where $\overline{x}$ and $\overline{y}$ specify the source location in the source plane, and Φ is the phase shift introduced by the object as defined in eq. (6). The integral is typically solved numerically, often using simplifying tricks (see, *e.g.* [11, 57]), and the squared modulus of the electric field as expressed by eq. (10) yields the X-ray intensity on the image plane.

Apart from the (typically negligible) blurring effect due to the finite computational grid adopted to solve eq. (10) numerically, this intensity will typically have the shape depicted in fig. 11(a): alongside the (extremely intense) main minima/maxima corresponding to the physical edges of the imaged object (see also fig. 9), a series of secondary minima and maxima will appear. However, this would correspond to a pattern generated by an "ideal" point source, and acquired with a detector device with virtually infinite spatial resolution: as a consequence, such a pattern is never observed in practice, as already pointed out since the early days of the approach [11, 58]. A simple way to take finite source size and detector resolution into account is to use convolution integrals [57, 59]: the pattern observed experimentally is obtained by convolving the "pure" pattern (as shown in fig. 11(a)) with the point spread function (PSF) of the used detector

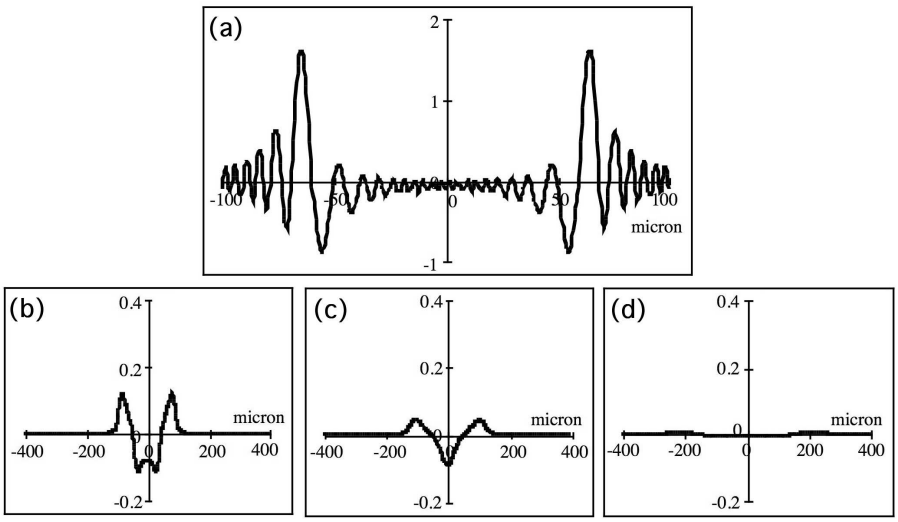

Fig. 11. – Effect of finite source size and limited detector resolution on the free-space propagation XPCi pattern.

and with the "re-scaled" source distribution ($s' = s \cdot z_{\mathrm{od}}/z_{\mathrm{so}}$ where s is the "physical" source distribution).

The PSF and s' can effectively be combined in a single "spread" function $S = \mathrm{PSF} * s'$ (where $*$ is the convolution operator), which effectively means that they have the same effect on the acquired image [60]. In fact, examples exist where either the blurring effect of the detector [61] or of the source [62] have been partly eliminated through deconvolution procedures, depending on which one was dominant. Panels (b), (c) and (d) in fig. 11 show the effect on the "pure" free-space propagation of a bell-shaped "spread" function S with FWHM equal to $50\,\mu$m, $100\,\mu$m and $300\,\mu$m, respectively. As can be seen, not only are the secondary phase peaks completely eliminated, but also the intensity of the primary peaks is severely affected, to the extent that they practically disappear when $S = 300\,\mu$m. This indicates the strong need for small focal spots and high detector resolution, which will be discussed in more detail in sect. **4**.

Observing the effect that the convolution with S has on the "pure" free-space propagation XPCi pattern enables an additional observation. It is in fact possible to re-draw fig. 9 based on the considerations used when fig. 7 was discussed, *i.e.* on the basis of eq. (9), which links the X-ray refraction angle to the gradient of the refractive index inside the sample. As said, this is maximal along the edges of the details, therefore leading to a situation like that (qualitatively) sketched in fig. 12. As can be seen, the effect of refraction at the edges is that of subtracting photons from the region immediately inside the object, leading to a reduction in the detected intensity *i.e.* a pair of negative peaks. These photons have not been eliminated, but simply redirected to the region immediately outside the detail, whey they add up to the undisturbed photons that travelled straight in the vicinity of the object. This creates a local increase in the detected intensity, *i.e.* a pair of positive peaks. Although the pattern calculated in this way cannot, for obvious reasons, reproduce the secondary phase peaks, its appearance is remarkably similar to that of *e.g.* the pattern shown in fig. 11(b), which was obtained by convolving the Fresnel/Kirchhoff diffraction pattern featuring all secondary oscillations

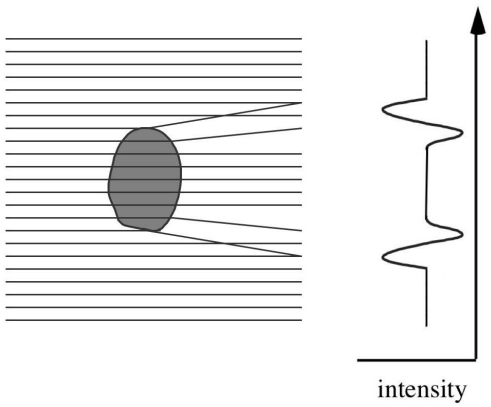

Fig. 12. – Ray-tracing interpretation of free-space propagation phase contrast imaging.

with a bell-shaped spread function S of appropriate width. In fact, papers like [18] and especially [17] demonstrate that, in cases of limited coherence, *i.e.* when laboratory sources, or even some synchrotron sources with limited coherence like bending magnets, are used, the simplified ray tracing and the more rigorous wave optics model yield indistinguishable results. Albeit there are examples in the literature that seem to suggest a separate treatment of "refraction" and "diffraction" effects (see, *e.g.* [63]), these are ultimately the same phenomenon, described by means of models with different degrees of approximation. While with high degrees of coherence the simplified ray-optics model breaks down and it is necessary to use the more rigorous wave optics approach (see, *e.g* [17,64]), they can be used interchangeably in cases where coherence is sufficiently low.

While the strict requirements on S, and therefore on s, imply that spatial coherence is a key parameter in free-pace propagation XPCi, the lesser impact of temporal coherence was observed since the early days of the method. In fact, Wilkins and co-workers' second *Nature* letter is based on free-space propagation images obtained with a micro-focal (to satisfy the spatial coherence requirements), but fully polychromatic, X-ray source [12]. Interestingly, images of similar quality were obtained previously by other researchers (see, *e.g.* [65]), who however did not interpret the substantially improved image quality in terms of phase effects.

Several authors studied ways to incorporate polychromaticity into image formation models (see, *e.g.* [60, 66]), and even used it to perform energy-based phase retrieval [67], albeit under a set of simplifying assumptions. Indeed, since the incoherent sum of the intensities is used in this case, polychromaticity can be included simply by means of a weighted sum over the spectral densities [60]. Excellent examples of recipes summarizing the effect of the various system parameters on key image metrics like contrast, signal-to-noise ratio (SNR) and resolution can be found in the work of Gureyev and collaborators (see, *e.g.* [68-70]).

Before developing his "energy-based" retrieval approach [67], Gureyev has been heavily involved in the development of quantitative phase approaches, practically since the origins of the method (see, *e.g.* [71, 72]). Phase retrieval methods for free-space propagation XPCi are many and diverse, and again listing them all would go beyond the scope of the present review; hence, we will name just a couple of significant examples.

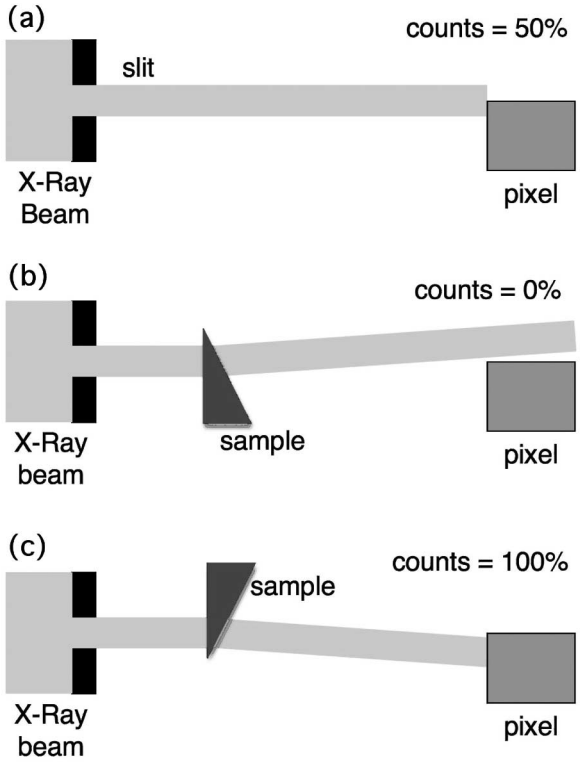

Fig. 13. – The basic principle of edge illumination phase contrast imaging.

Cloetens' "holotomography" approach, still widely used, links retrieval and CT and requires a sequence of projection images acquired at a range of z_{od} values [73]. Paganin and co-workers, by imposing the strong constraint that the sample should be made of a single material, developed a retrieval approach that requires the acquisition of a single image [74]. The great advantage of requiring a single input image, jointly with the fact that the algorithms often yields satisfactory results also if the above condition is partly violated, probably makes it the most widely used phase retrieval method.

Similarly diversified are extensions to CT, which date back to the origins of the method (especially at the ESRF, see, *e.g.* [75-77]), with subsequent significant contributions to quantitative aspects provided by Bronnikov [78], Barty *et al.* [79], and many others. Even more diverse is the range of pursued applications, for which we refer the reader to the quoted reviews [8,9] as well as [80-84]. Interestingly, mammography has been one of the first medical applications to be pursued, in particular by the Trieste group [57,85], which will be the subject of sect. **3**.

2˙4. *Edge illumination.* – Edge Illumination (EI) XPCi was developed at Elettra in the late '90, as an alternative to ABI that does not require the use of an analyser crystal [15].

The basic idea is to illuminate only one edge of the detector pixels, as schematized in fig. 13(a). Imagine that the schematized set-up extends indefinitely in the direction entering the plane of the drawing. The beam is shaped by a slit to be very thin in

the vertical direction, and to extend sufficiently to cover the full extent of the object in the horizontal one. The detector consists of a single row of pixels, as large as the beam in the horizontal direction. As often done in synchrotron experiments, 2D images are then obtained by scanning the sample vertically through the beam, reading out an image line at each object position, then combining these lines to form the image. The main difference in this case is that the beam, rather than matching the detector active surface or at least hitting it in the centre, hits the edge of the pixel array. In this way, when no object is present (fig. 13(a)), the detector counts 50% (or any given percentage, depending on the relative shift between beam and detector) of the primary photons. This situation is effectively equivalent to positioning an analyser crystal between sample and detector tuned at 50% reflectivity. When an object is introduced, any gradient in its refractive index will cause refraction *i.e.* induce a beam deflection (for simplicity's sake, in the figure the object is represented as a wedge inducing a uniform refraction angle across the beam, and the angle itself has been highly exaggerated). An upward deflection (fig. 11(b)) will cause a reduction in the number of detected photons, *i.e.* a negative fringe in the image; conversely, a downward deflection will result in the detection of more X-rays *i.e.* a positive fringe. For example, if a cylindrical fibre (entering the plane of the drawing) is scanned across the beam, an image analogous to that showed on the right-hand side of fig. 8 is obtained. It can also be shown that, if one adjusts the vertical beam dimension and/or the value of z_{od} so as to obtain the same angular selectivity (*i.e.* achieve the same phase sensitivity) as a given crystal reflection, identical images are effectively obtained. This analogy with ABI, already pointed out in the original EI paper [15], was recently formally demonstrated [86]. Although the method maintains common features with free-space propagation (an equivalent interpretation is to imagine a version of fig. 12 where all X-rays that do not contribute to the signal are eliminated: for more details see [87, 88]), it is easy to see that it fully decouples the intensity of the signal from the spatial resolution of the detector [15]. For example, with reference to fig. 13, one could imagine extending the vertical dimension of the pixel downwards indefinitely (leading to an arbitrarily large PSF): so long as the beam keeps hitting the top edge of the pixel, the detected signal would not change.

The synchrotron EI set-up offers a number of additional options. For example, shifting the beam further upwards with respect to fig. 13(a), so that it just misses the detector active surface, leads to a form of "single-shot" dark field imaging [89]. Clearly one can use detectors consisting of more than one row of pixels [90], and through the design of appropriate masks [91], simultaneously acquire absorption, phase contrast and dark field images by means of a single scan of the sample through the beam [92, 93].

More recently, as a result of a collaboration among three synchrotrons (Elettra, Diamond and the ESRF), the method has been the subject of intense investigation, which demonstrated a number of significant features. First, that the method allows fully quantitative phase retrieval through the acquisition of only two images [94], obtained by illuminating the opposite edges of the pixel: this effectively inverts the differential phase signal, while absorption remains the same, similarly to what happens in ABI when opposite sides of the crystal rocking curve are used. Secondly, it was show that the method is highly robust against increasing X-ray energy, to the extent that it can provide image contrast tens of times higher than other XPCi approaches as energy is increased [95]. Third, and possibly most importantly, it was proven that, if the set-up is optimized and the phase retrieval method further developed to include coherence effects [64], the method outperforms other differential XPCi approaches in terms of phase sensitivity, by at least one order of magnitude [64, 96, 97].

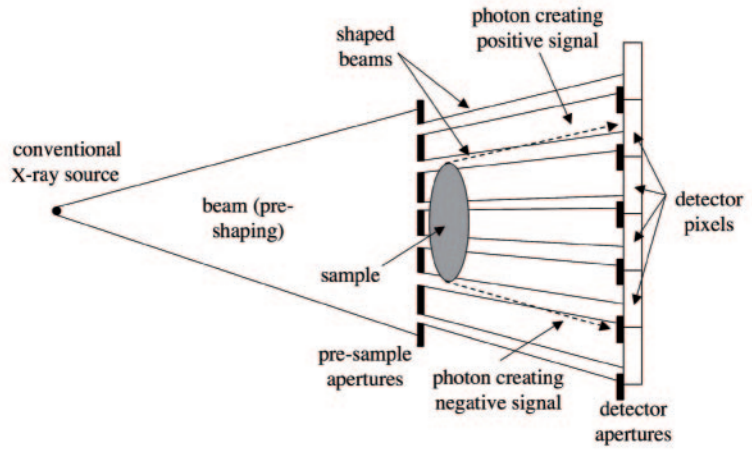

Fig. 14. – Schematic representation of the lab implementation of edge illumination phase contrast imaging (sometimes referred to as "coded-aperture" XPCi).

The other key aspect enabled by the fact that EI is effectively a "crystal-less" ABI approach is that, unlike in real ABI, divergent and polychromatic beams can be used. This enables adaptation for use with conventional sources, which was achieved by means of a pair of opportunely designed masks [98, 99] (sometimes called, possibly slightly improperly, "coded-aperture" masks). Figure 14 shows a schematic side view of the imaging system, where once again one should imagine the set-up extending in the direction entering the plane of the drawing. The two masks are identical, apart from a scaling factor that accounts for the beam divergence. The larger one is placed in contact with the detector, and its only purpose is to create insensitive regions between adjacent pixels (*e.g.* it could be eliminated by using specialized detector technology, or it could be directly laminated onto the detector device). The downscaled mask is placed immediately before the imaged sample (therefore protecting it from unwanted dose delivery), and it serves the purpose of creating an array of physically separated "beamlets". Each beamlet hits the transition region between a sensitive and an insensitive area on the detector array, therefore replicating the situation schematized in fig. 13(a) for each row of an area detector. The availability of many beams effectively replaces the scanning needed at synchrotrons: here the sample is simply placed downstream of the first mask and imaged. If no phase retrieval is required (see below), the method is effectively single shot.

Early simulations developed before the system was realized in practice [99] predicted a negligible decrease in the detected (differential) phase signal for focal spots of up to at least $100\,\mu$m. Given the method's links with free-space propagation [87, 88], and considering the high sensitivity of the latter to increasing focal spot sizes, this was under many respects an unexpected outcome, which was however repeatedly demonstrated experimentally [98-101]. Data analysis and critical review of the methodology led to the conclusion that there are two reasons behind this robustness, which are:

1) The method is completely non-interferometric and purely based on the detection of refraction, which survives under relaxed coherence conditions [17, 18, 102], although it becomes more difficult to detect. The shifted mask arrangement enables its efficient detection despite the lack of coherence, by significantly reducing the undeviated background [87].

2) Possibly most importantly, the pitch of the apertures is relatively large. As discussed above, the disruptive effect of an increasing focal spot is expressed in terms of projected source size $s' = s \cdot z_{\mathrm{od}}/z_{\mathrm{so}}$ where s is the "physical" source distribution. In our current lab set-up, $z_{\mathrm{od}} = 0.4\,\mathrm{m}$ and $z_{\mathrm{so}} = 1.6\,\mathrm{m}$, hence a "physical" source size of $100\,\mu\mathrm{m}$ leads to a source-induced blurring of approximately $25\,\mu\mathrm{m}$. If a pixel size of $100\,\mu\mathrm{m}$, or even close to $\sim 50\,\mu\mathrm{m}$, is used, this is smaller than the separation between two adjacent beamlets, and so long as the beamlets remain physically separated, the edge illumination condition can still be realized, which means that the method still works.

This further demonstrates the very basic physical difference between the incoherent EI method and coherent methods like for example grating interferometry (see next section). In that case, the (equivalent of the) beamlets must overlap and interfere for the method to work, which only happens if the phase grating is illuminated coherently. In the EI case, the beams are deliberately kept separated so that interference is avoided (moreover, the pre-sample mask is illuminated incoherently, which would make interference effect undetectable anyway).

One simple and effective way to understand the limited impact that spatial incoherence has on the EI method (for a detailed technical discussion see ref. [102]) is to represent it as a broadening of the beamlets hitting the transition between sensitive and insensitive regions on the detector mask. With reference to fig. 14, one should imagine the vertical profiles of the individual beamlets hitting the detector masks being described by the convolution between the projection of the apertures in the pre-sample mask with a $25\,\mu\mathrm{m}$ FWHM Gaussian (rather than simply by the (sharply shaped) former, as is depicted in the figure for simplicity's sake). So long as the beamlets are physically separated, also if the projected focal spot dominates *i.e.* the footprint of each beamlet on the detector mask becomes virtually Gaussian, by chopping each beamlet in half with the edge of a detector aperture, one still remains highly sensitive to any vertical displacement of these (blurred) beamlets.

This is also what enables the lab-based version of the phase-retrieval method to provide, within the obvious "effective energy" constraints common to all methods using polychromatic radiation [103], results in many cases indistinguishable from their synchrotron counterpart [104]. Like in the synchrotron case, phase retrieval is performed by processing two frames acquired while illuminating opposing sensitivity edges, in this case two edges on the same detector aperture [86, 104, 105]. In the situation shown in fig. 14, this is obtained simply by acquiring a first frame in the depicted configuration, and a second one after the pre-sample mask has been moved upwards by one (demagnified) detector aperture.

The interesting aspect here is that, jointly with the above discussed insensitivity to increasing pixel size, this effectively means that the EI method removes the main limitation of free-space propagation XPCi, *i.e.* the rapidly decreasing signal with increasing $S = \mathrm{PSF} * s'$ (see fig. 11 and related discussion). In fact, increasing the pixel size (or simply the pitch of the masks) would enable using even larger focal spot sizes, albeit at the expense of spatial resolution. This, however, could be recovered by means of "dithering" methods [98-100, 106], at least in those cases where exposure time is not too stringent a requirement.

Additional advantages of the method are robustness against environmental vibrations [100, 107], and, like its synchrotron counterpart, against increasing X-ray energy [101]. Reference [101], as well as [108], also shows direct examples of how EI outper-

forms free-space propagation for the same experimental set-up, while refs. [15,95,109] do the same for the synchrotron case. To the best of our knowledge, ref. [109] also provides the first example in which a differential XPCi method was made sensitive to phase effects in two orthogonal directions simultaneously, in this case by using L-shaped pre-sample apertures instead of long slits, and aligning both sides of each L shape to two orthogonal edges of the corresponding (square) detector apertures.

While one could be erroneously led to think that the large aperture pitch reversely affects the method's phase sensitivity, it was recently proven that this is not the case, and that in fact the pitch of the apertures has no influence on the sensitivity [110]. Indeed, the same sensitivity as grating interferometry is achieved, despite the highly simplified set-up.

More recently, it was demonstrated that quantitative dark field approaches are also accessible by acquiring one additional image [111], *i.e.* three frames instead of two as required by the "standard" phase retrieval method, and CT developments are currently underway, with the first examples of having appeared in recent conference proceedings [96,112].

Like for previously discussed XPCi methods, providing a complete list of applications which has been targeted by means of EI lies beyond the scope of this review, however this is long and diverse and includes security scans [113-115], small animal imaging [116-118], mammography [119], palaeontology [95,96], material science [120], and others.

2˙5. *Talbot and Talbot-Lau (or "grating") interferometry.* – The last XPCi approach to have emerged (in the early '2000) is Talbot (or "grating") interferometry (see fig. 15). It exploits the phenomenon of Talbot self-imaging, on the basis of which, when a grating is coherently illuminated, diffraction patterns that are an exact replica of the grating that created them are observed at a given set of (Talbot) distances [121]. A phase grating is often used to produce the self-images; by placing an absorption ("analyser") grating at one of these "Talbot" distances, any perturbation of the pattern caused by the introduction of an object along the beam path can be sensed, and related back to the object itself.

This is a well-known method in optics, which became available also at X-ray wavelengths at the end of the last millennium, thanks to the advancements in nanofabrication techniques that enabled manufacturing gratings with a sufficiently small pitch. Following pioneering investigations by Cloetens *et al.* [122,123], proof-of-concept results were published in rapid succession by David *et al.* first [124], and by Momose *et al.* shortly afterwards [125]. The method then developed quickly, resulting, *e.g.*, in the production of the first CT images [126], and experienced a sudden surge of popularity when Pfeiffer *et al.* demonstrated that a conventional X-ray source could be used by adding a source grating [127], *i.e.* switching from the Talbot to the Talbot-Lau configuration [128]. As discussed above, the phase grating needs to be illuminated coherently in order to produce the self-images at the basis of the method itself: the source grating "slices" the extended source in an array of mutually incoherent, but individually coherent "sourcelets", thus providing said coherent illumination. The lab-based implementation was also rapidly translated to CT [129], after which another extremely popular paper was published, again by Pfeiffer *et al.*, which extends the method to dark field imaging [130]. This was based on an extension of the analysis carried out up to that point on "phase stepping" curves to perform phase retrieval. A "phase stepping" curve is obtained by laterally shifting one of the gratings with respect to the others, in (typically 8-10) sub-pitch steps, in the direction orthogonal to the trenches (*i.e.* vertically with reference to fig. 15). This yields a pixel-by-pixel quasi-sinusoidal curve, the lateral shift of which is associated with

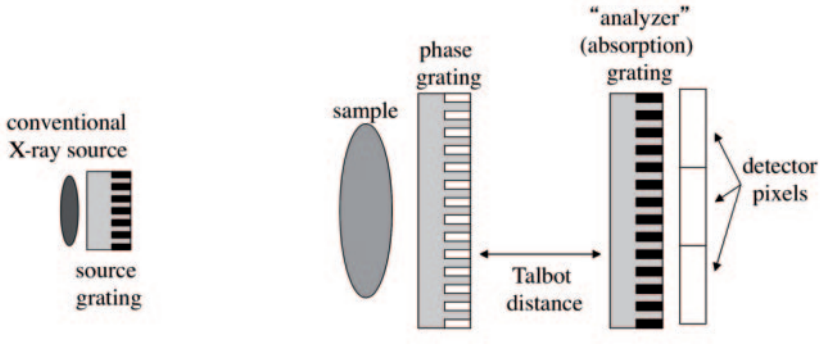

Fig. 15. – Schematic of the Talbot-Lau interferometer. The Talbot interferometer is obtained simply by removing the source grating: in that case, a spatially coherent source must be used.

the local change in differential phase, while the reduction in average intensity provides absorption. Pfeiffer *et al.* observed that, as well as the shift and the intensity reduction, a "dampening" of the oscillation is also observed, that can be linked to the dark-field imaging signal generated by the sample. This is equivalent to the "broadening" of the crystal rocking curve observed 5 years before by Rigon, Pagot, Oltulu and respective co-workers [44-46], and is in fact linked to the same physical quantity.

The popularity of the method means that it is undergoing continuous development, including 2D grating schemes [131,132], interlaced acquisition modalities aimed at saving acquisition time when the phase stepping procedure has to be coupled with sample rotation in CT [133], in-depth analysis on the origins of the dark-field signal [134] and much more. The range of targeted applications is even more varied, and listing them again goes beyond the scope of the present work; for details, the reader is referred to a recent review by Pfeiffer *et al.* [135].

2˙6. *Other approaches.* – An interesting variation on the grating method was introduced in 2008 by Wen and co-workers [136]. They proposed the use of a single absorption grating (*e.g.* a standard anti-scattering grid), and a Fourier-based analysis method to separate the various sample-induced signals with a single shot. The method has significant advantages, *e.g.* it enables placing the grating before the sample with consequent dose saving, and it is easily extendable to 2D implementations [137]. Albeit the approach comes at the price of a reduced resolution and probably sensitivity, it proved capable to extract significant bone structural information [138]. Wen's following effort was the equally interesting development of an interferometer with sub-micron pitch gratings [28], the use of which resulted in a hybrid between grating and Bonse/Hart interferometry which, although at the moment possibly limited in terms of practical implementations, yields great promise for increased phase sensitivity.

Huang and co-workers proposed a variation on grating interferometry where only absorption gratings are used; these have a larger pitch than standard gratings, and the geometrical penumbra from the first grating is used to replace the Talbot self-image [139]. The method could be seen as a hybrid between grating interferometry and the lab implementation of edge illumination; however, it still relies on the phase stepping mechanism to extract quantitative parameters. As such, it does not exploit the enhanced phase sensitivity yielded by the edge illumination condition: although in some of the phase

stepping positions this might effectively be realized, the overall sensitivity is washed out by the other positions of the phase stepping curve, at which the sensitivity is lower. A similar approach was also proposed a few years afterwards by Choi and Park [140].

Much more could be mentioned, such as for example Pellicia and Paganin's clever idea to use the edge of a mirror as a sensing device [141], or Nesterets and Wilkins' approach in which two gratings are simultaneously scanned [142]. A number of interesting alternative approaches have also emerged that however require very high-resolution detectors, which could be a limitation in terms of clinical translation. Among these are for example single-grid methods, where the refraction caused by the sample is analysed in terms of projected grid displacements [143]; interestingly, this type of studies led to the tantalizing observation that a simple sheet of (sand)paper can be used to replace the grid itself [144]. More examples could be quoted, which however belong primarily to the realm of early, proof-of-concept synchrotron experiments, and are therefore slightly out of scope for a "translational"-oriented review like this one. This notwithstanding, we find it interesting that the area is still extremely vital and bubbling with new ideas: these could lay the foundations for future translational exercises, and the overall feeling is that the field of XPCi might still provide significant surprises in the near future.

3. – X-ray phase contrast mammography: the world-leading experience developed in Trieste

3˙1. *The history of the project.* – The proposal to build a Synchrotron Radiation (SR) facility, later named Elettra, was launched during the 71st Annual National Congress of the Italian Physical Society, in October 1985 in Trieste, Italy. Several meetings — generally held at *The Abdus Salam* International Centre for Theoretical Physics (ICTP) in Trieste— immediately focused on the issue of which beam lines had to be developed. Preliminary conclusions were presented at a workshop in May 1987, at ICTP, where mammography was just mentioned [145]. A new company, named Sincrotrone Trieste SCpA (ST), devoted to the construction of the Elettra laboratory, was established in those years.

The SYRMEP (SYnchrotron Radiation for MEdical Physics) Project, for the construction of a medical beam line, already foreseeing the final phase of "*in vivo*" mammographic examinations, was presented at a meeting of the Program Advisory Committee of ST at the National Research Council (CNR) in Rome in September 1991. The project approval was subject to the fulfillment of two conditions: finding the necessary funds and starting with the "*in vitro*" phase, in order to verify the effectiveness of the proposed technique.

Elettra began its operations in 1993, and in the same year the construction of the SYRMEP beam line started off. The University of Trieste (UTS) was the major source of funding, with a significant contribution from ST; in addition, the National Institute of Nuclear Physics (INFN) supported the development of a new digital detection system.

The "*in vitro*" experimentation started in 1996 and the results of this preliminary phase were very promising. Two years later, the international scientific committee of ST approved the next steps of the "*in vivo*", *i.e.* with patients, experimentation, provided that the availability of funds was secured.

In the next year the Fondazione CRTrieste agreed to financially support the project, formally called "Synchrotron X-ray mammography: clinical experimentation". Since experiments on patients were envisaged, the UTS and the local Hospital on one side, and the ST on the other, signed a five year agreement. The INFN continued to support

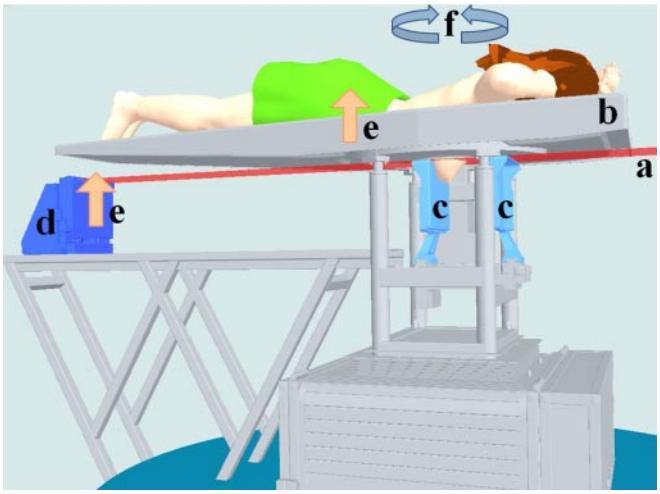

Fig. 16. – Sketch of the imaging system for phase contrast mammography with synchrotron radiation: (a) stationary and laminar X-ray beam, (b) movable patient support, (c) compression system, (d) holder for screen-film cassette, (e) vertical scanning movement of the patient and of the screen-film system through the beam, which allows the acquisition of planar radiographic images, (f) rotational movement of the patient, which allows both the craniocaudal and mediolateral oblique views to be obtained. Reproduced, with permission, from Castelli *et al.* *Radiology*, **259** (2011) 684 (supplementary material).

the digital detection system, also in view of possible developments in the field of tomomammographic experiments.

The beam line modification phase started in 2000 by designing the patient room with the micrometric precision patient scanning support, the room for radiologists and radiographers, and the control system to comply with all the required safety regulations. In July 2004 the Ethical Committee of the local Hospital authorized the experimentation on patients. In the next year, an Italian ministerial agency run a dry test on the general safety control system, leading to positive feedback; a renewed five year agreement of the three contracting bodies defined the performances to be attained and the responsibilities of the persons involved in the experimentation. Eventually, in January 2006, the Ministry of Health gave the ultimate approval.

A description of the original beam line can be found in [34]. The upgrade in view of experimentation with patients on the clinical mammography system is shortly discussed in [146,147], and a sketch of the experimental setup including the patient's bed is shown in fig. 16. This upgrade left the pre-existing experimental room for standard SR experimental activities unaffected, when the patient modality is not active.

In March 2006, the first phase of *in vivo* mammographic examinations at the SYRMEP beam line commenced, using screen-film systems as detectors. Results from the first nine patients were presented at the X Pisa Meeting (2006) [148]. In December 2009 the first phase of the clinical experience with 71 patients was completed, and in June 2011 the results for the first 49 patients (March 2006 - September 2007) were published in *Radiology* [149]. Finally, in February 2013, the results of the qualitative analysis on the complete patient cohort were presented at the Royal Society scientific meetings "Taking X-ray phase contrast imaging into mainstream applications" [150], and the conclusive quantitative analysis is reported in the present paper.

3˙2. *Breast cancer*. – Among women-specific diseases, breast cancer has become one of the leading causes of death globally. It has been estimated that one in 12 women will develop breast cancer at some stage in her life, owing to risk factors such as hormonal effects, age and genetic predisposition.

In Europe, breast cancer has been the most commonly diagnosed form of cancer. Though the incidence rate has significantly increased, there has also been an increase of treatment and survival rates; from this point of view, the agreement among the medical community is that early diagnosis of breast cancer has direct beneficial consequences on a successful prognosis: early detection saves lives. The first-line approach to the early diagnosis of breast cancer is mainly based on X-ray mammographic examinations.

Mammography, however, is far from being perfect. Its diagnostic performance may depend on several factors, and is reported to have sensitivity between 60% and 90%, and specificity between 80% and 95% [151, 152]. The reported positive predictive value is usually in the order of 10% [153, 154], implying that for each true-positive patient, nine false-positive patients are sent to further diagnostic investigations.

In Appendix A, sensitivity and specificity are defined, discussing the role of the 2×2 contingency table in the specific case of mammography, and elucidating the intrinsic difficulties of this clinical diagnostic test.

The detection and characterization of breast abnormalities, including opacities, architectural distortion and microcalcifications, is in fact a most challenging task due to their frequent small size and limited conspicuity relative to the surrounding anatomical structures of the breast. Small or indistinct breast lesions are often visible retrospectively when reviewing the patient's previous examinations, but identifying them prospectively remains difficult.

The early diagnosis of breast cancer requires in particular the detection of microcalcifications (high-contrast, small-size details) and nodules (low-contrast details). The visibility of these details depends on object size, object contrast and X-ray intensity. Small-size and low-contrast features require high radiation dose for a good image quality to be achieved. However, since breast is one of the most radiosensitive organs, the risk of radiation-induced cancer needs to be minimized. Increasing image quality without increasing the dose is therefore one of the primary goals in mammography.

Initial X-ray mammography is often accompanied by ultrasonography (US). However, since the number of false-positive results is high, there is a strong demand for a second-line investigation capable of substantially reducing this number. Various methods have been developed over the years to address these limitations in mammography, achieving varying levels of success [155, 156].

Mammography with synchrotron radiation (MSR) is an innovative X-ray imaging technique that may be utilized to improve the identification of breast lesions. Synchrotrons provide X-ray beams which are practically monochromatic, tunable (thus enabling dose optimization), laminar (determining a general reduction in scattered radiation) and with sufficient spatial coherence to allow the exploitation of phase effects [8, 9, 82, 157]. Given these conditions, XPCi can be performed at high contrast and spatial resolution, even with reduced doses.

Previous studies have extensively discussed the improvement in image quality provided by phase contrast MSR in phantoms or surgical specimens of the breast [34, 35, 49, 50, 57, 158-161]. The results of these *in vitro* studies proved so encouraging that a clinical program was launched, in what is effectively the final phase of the previously introduced SYRMEP Project [148].

Until now, X-rays from synchrotrons have been used in digital coronary angiography

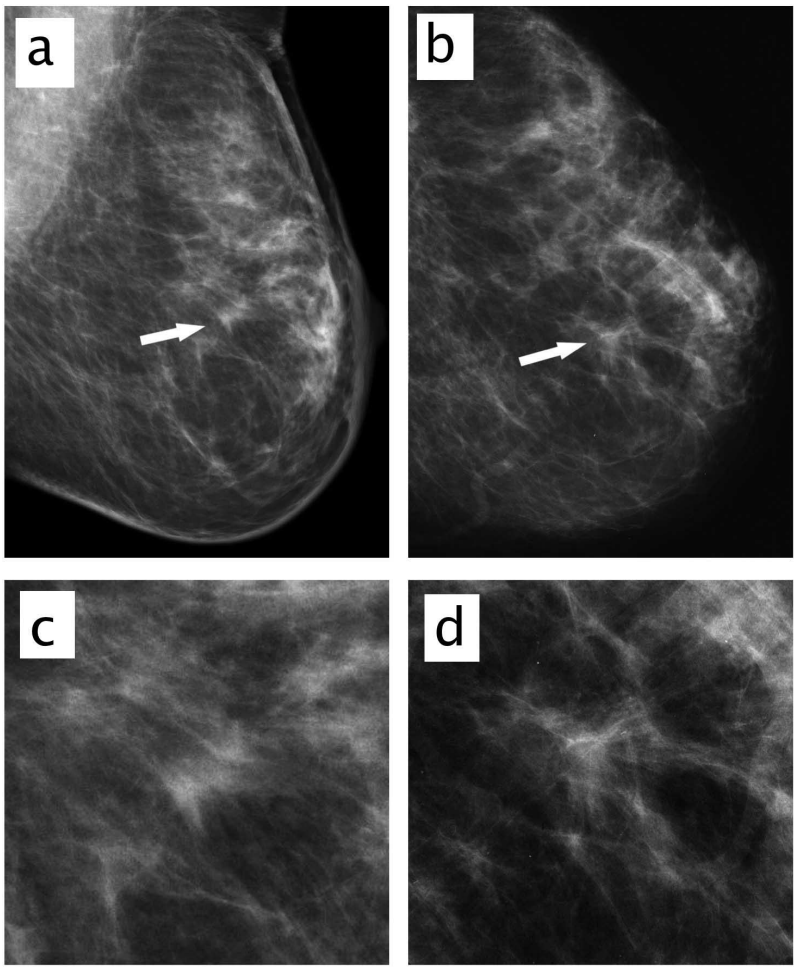

Fig. 17. – Images of left breast in 62-year-old woman with suspicious mass identified at DM. (a) Mediolateral oblique DM image and (c) corresponding digital zoom image show suspicious mass (arrow) with speculated margins (BI-RADS category 4) in retroareolar region. (b) Findings on synchrotron radiation mammographic image and (d) corresponding digital zoom image confirm and better depict the spiculated mass (BI-RADS category 5). Reproduced, with permission, from Castelli *et al. Radiology*, **259** (2011) 684.

examinations conducted on 470 patients between 1979 and 2000 [162, 163]. However, no previous studies have analyzed the diagnostic capabilities of phase contrast MSR in a patient study. The purpose of this study was therefore to assess the diagnostic contribution of phase contrast MSR in patients with suspicious breast abnormalities on first-line mammography or mammography combined with US.

3˙3. *Data analysis*. – The study involved 71 patients with unresolved breast abnormalities after conventional digital mammography (DM) and ultrasonography exams carried out at the Radiology Department of the University Hospital of Trieste, in the years 2006-2009. All patients were subjected to both examinations, and still the diagnosis remained

unresolved. All details about this clinical research can been found in [149]. However, while in that paper results form the first 49 patients were reported, here we present the analysis for the full cohort (69 instead of 71 patients in total, since 2 did not complete the protocol). These cases were referred for mammography at the synchrotron radiation facility, with images acquired using propagation-based XPCi (see above). Their average age was 59.3 years, with a standard deviation of 9.1 years.

As a first step to investigate the contribution of phase effects to image quality, two experienced radiologists, specialized in mammography, assessed the visibility of breast abnormalities and of breast glandular structures, by looking at the hospital and the MRS images of the same case side by side. Images were compared, and graded according to a relative seven-grade visual scoring system. This led to the conclusion that phase contrast MSR depicts normal structures and abnormal findings with higher image quality with respect to conventional digital mammography [150]. An example of the difference in image quality between conventional and MSR is shown in fig. 17.

In a separate session, the two readers assessed all images (MSR and conventional) independently, and rated them according to the BI-RADS categories [164]; these BI-RADS scores were then dichotomized such that scores of 1-3 were considered to indicate negative result and score of 4-5 were considered to indicate a positive result [149].

This scoring system enabled analyzing the data with the 2×2 contingency table discussed in Appendix A. In fact the negative or positive result of the specific diagnostic test can be compared with the final diagnosis (negative or positive to the disease) provided by the result of the biopsy or the follow-up at one year. Two patients did not complete all the steps of the protocol and were thus excluded from the final analysis; therefore the 2×2 tables refer to 69 patients. It should be noted that, for all patients, the delivered radiation dose was lower or equal to the dose administered in a standard clinical DM procedure. Full details on how the irradiation parameters were fixed and how the dose was calculated are provided in ref. [149].

3˙4. *Result and discussion.* – Table I shows the 2×2 contingency table for the conventional digital mammography and for the phase contrast MSR.

The results of the comparison between the two techniques are reported in table II,

TABLE I. – 2×2 *contingency tables for hospital-based full-field digital mammography (upper part) and synchrotron radiation phase contrast mammography (lower part).*

Digital Mammography			
	Ill	Healthy	
DM positive	23	19	42
DM negative	6	21	27
	29	40	69
Phase contrast MSR			
	Ill	Healthy	
MSR positive	25	2	27
MSR negative	4	38	42
	29	40	69

TABLE II. – *Comparison between full-field digital mammography and synchrotron radiation phase contrast mammography.*

	DM			MSR		
	Num	Den	Num/Den	Num	Den	Num/Den
Prevalence	29	69	0.42	29	69	0.42
Sensitivity	23	29	0.79	25	29	0.86
Specificity	21	40	0.53	38	40	0.95
PPV - Positive predictive value	23	42	**0.55**	25	27	**0.93**
Pearson Chi-square			7.14			46.55
Two-tailed Fisher exact probability			0.012			< 0.000001

with the various quantities (*e.g.* the PPV-positive predictive value) being introduced and discussed in Appendix A.

Finally, the stratification according to agreement/disagreement between conventional digital mammography and for the phase contrast MSR radiation is shown in table III.

For 48 patients, 25 ill and 23 healthy, DM and MSR are in agreement; however, 3 ill patients are negative to both tests, and 2 healthy ones are positive to both tests.

On 21 patients, 4 ill and 17 healthy, DM and MSR are in disagreement; all the 17 healthy patients are positive for DM and negative for MSR. For the 4 ill patients, 3 are positive and 1 negative for MSR.

The disagreement on the 17 healthy patients, positive for DM and negative for MSR, is the main difference between the two tests, with MSR providing the correct result; for the 4 ill patients, the MSR results are also better, with more cases identified as such. Of course, the 5 cases of disagreement between the tests and the final diagnoses and the 4 ill patients with different results in DM and MSR require further analysis, and show that the method is still susceptible to improvement.

TABLE III. – *Stratification according to agreement/disagreement between conventional digital mammography and phase contrast MSR.*

Agreement between DM and MSR			
	Ill	Healthy	
DM and MSR positive	22	2	24
DM and MSR negative	3	21	24
	25	23	48
Disagreement between DM and MSR			
	Ill	Healthy	
MSR positive	3	0	3
MSR negative	1	17	18
	4	17	21

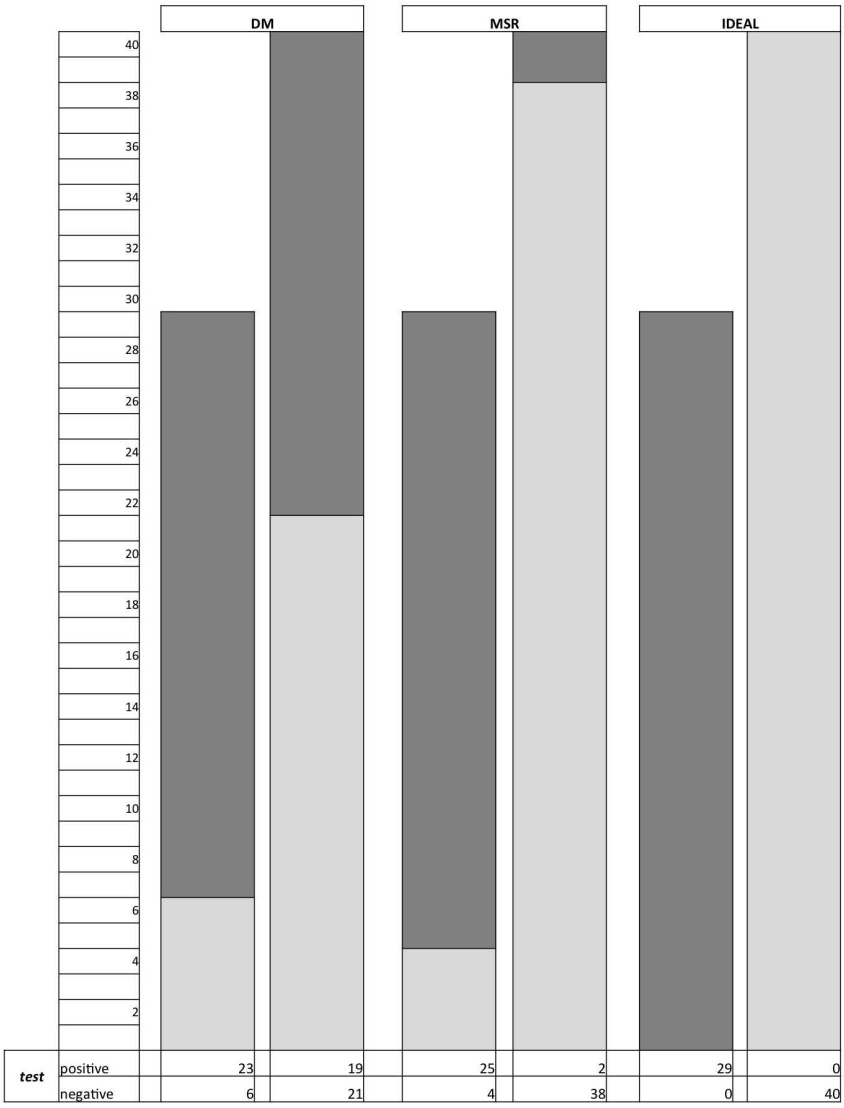

Fig. 18. – Histogrammatic representation of the 2×2 contingency table. The numbers reported below the three tests provide the figures of the corresponding table. For all pair of columns *i.e.* for each test, the column on the left-hand side represents the diseased patients, the one on the right-hand side the healthy ones.

It should be noted that conventional DM is a first-level exam. At this level, there is great demand for a substantial improvement in sensitivity. At a second level, *i.e.* after an initial mammography, the significant number of false positives requires a targeted strategy for their reduction, which would also lead to a corresponding reduction of cyto-histological analyses (biopsies).

The results reported above suggest that phase contrast MSR could be used for this aim, *i.e.* to clarify cases of questionable or suspicious breast abnormalities identified at previous digital mammography exams.

In terms of patient care implications, phase contrast MSR has the potential to be a second-level examination after mammography, with the aim of reducing the number of diagnostic biopsies performed.

Figure 18, actually a graphical representation of the 2×2 contingency table, summarizes all previous considerations, apart from the Pearson Chi-square or the Two-tailed Fisher exact probability, which are computed with more complicated procedures that refer to the respective null test (see Appendix A).

In the figure the true positives to the specific test are in dark grey, while the true negatives are in light grey. Taking into account the ideal test, it is apparent that, in our sample, phase contrast mammography with synchrotron radiation behaves better than conventional digital mammography, with the largest difference being observed for healthy patients.

4. – Beyond synchrotrons: current opportunities for clinical translation

Together with the many quoted examples where XPCi was demonstrated to outperform conventional X-ray methods on *in vitro* tissue samples, the Trieste experience discussed in the previous chapter proves beyond doubt that XPCi can be extremely beneficial in real *in vivo* medical investigations. However, not only are synchrotrons —for obvious reasons— not suitable for widespread clinical use; their very nature also limits the type of *in vivo* studies that can be performed. In this sense, the Trieste case is exemplary: the team only had access to patients who already underwent a conventional examination, and for whom this did not result in a definitive diagnosis. Presented with this patent cohort, the Trieste study successfully reduced the number of false positives *i.e.* demonstrate an increased specificity. However, it could be argued that reducing the number of false negatives would be even more important. This requires examining a much larger population of (typically asymptomatic) patients in a screening study, which would be much more difficult to perform at a machine with a limited capacity like a synchrotron. To make this happen, XPCi needs to be taken out of synchrotrons and specialized labs, and into mainstream applications: the benefits of this would extend well beyond mammography as well as beyond medicine itself, and have been the subject of a recent discussion meeting held at the Royal Society in London [165], the proceedings of which are an immediate reference for the reader who wishes to expand on the subject.

The first hurdle that needs to be overcome to achieve such a translation is the effective implementation of XPCi outside SR sources. This can be based on two approaches: the development of new X-ray sources, in which higher coherence is made available without excessively reducing the available flux, or the development of XPCi methods that do not rely on coherence, and can thus be implemented with existing X-ray sources.

4˙1. *New X-ray sources.* – This is a wide and diverse area, with extremely exciting possibilities been offered by inverse Compton approaches [166-169], laser plasma, the use of which was proposed already in the early days of XPCi [170], and which has more recently demonstrated very exciting possibilities [171-173], compact synchrotrons [174], and others; a thorough discussion of which lies beyond the scope of this review. For our purposes, it should be noted that, also when in principle commercially available, these sources seem not to be sufficiently perfected yet (and in fact there is an extensive, fully justified research activity still underway), and their current prospects in terms of cost and dimensions are such that, for the time being, one could only envisage some sort of

"specialized" use —*e.g.* large hospitals having one such source, used only for a certain class of specialized exams.

Somewhere in between new approaches and more traditional sources is the recent development of a liquid jet source, where the continuous "renovation" of the target material allows overcoming the intrinsic limits associated with maximum heat loads caused by electron beam bombardment [175]. At present, however, the technology seems to be restricted to small focal spots, which, while possibly viable for *e.g.* small-animal imaging [176], do not yet allow the sort of fluxes required in clinical applications.

Arguably the most attractive aspect that would be offered by new source technologies offering both high spatial coherence and high flux, is that they would enable using the free-space propagation approach, which, as discussed in sect. **2**˙3, is the simplest XPCi implementation since it does not require masks, crystals or gratings. In fact, this simplicity has already attracted significant interest, and has made it the subject of the only attempt at (non-synchrotron) clinical translation of XPCi. However, its significant dependence on spatial coherence (see fig. 11 and related discussion) meant that its use in combination with source sizes large enough to be clinically viable led to negligible phase effects in the acquired images, ultimately resulting in "no statistically significant difference in recall rates and cancer detection rates when compared with conventional film screening" [177]. Indeed, the substantial limitations in image improvement that are obtained when free-space propagation XPCi is used in combination with clinically viable source sizes were known since the early days of the method [178].

4˙2. *XPCi with existing sources.* – While there is little doubt that new source technologies will play a very important role in the future of medical imaging, a more rapid translation would need to be based on XPCi methods which rely less on coherence, and therefore have a chance to be implemented with existing source technologies.

While this rules out free-space propagation (for the reasons outlined above) and, for even more obvious reasons, Bonse/Hart interferometry, it was observed that Analyzer-based imaging can function under more relaxed spatial coherence conditions [179]. However, the introduction of a crystal automatically implies the selection of a very narrow energy bandwidth, which again corresponds to a very inefficient use of the flux provided by a conventional X-ray source. In fact, while translation attempts exist [180], these are characterized by excessively long exposure times, to the extent that the use of multiple X-ray sources has been taken into account as a possible solution to the problem.

Still on the use of incoherent sources, enthusiasm was generated in the mid'00s by Pfeiffer *et al.*'s demonstration that, thanks to recent developments in grating fabrication, Talbot-Lau interferometers could be implemented at X-ray wavelengths [127]. This built on the previous work of David *et al.* [124], Momose *et al.* [125] Weitkamp *et al.* [126] and others, who demonstrated the same principle in the Talbot configuration, using coherent synchrotron X-rays. As already mentioned, the method in itself remains a coherent one: no Talbot self-images are generated by a grating that is illuminated incoherently. What happens in the Talbot-Lau case is that the introduction of the third, "source" grating generates sufficient (spatial) coherence by collimating the extended source, along the same lines applied to *e.g.* free-space propagation XPCi through the use of a multiple-pinhole source collimator [181]. While this effectively allows the use of an extended source, it has the downside that a large fraction of the source is covered by the absorbing part of the source grating (which typically has a less than 50% open fraction), intercepting

the majority of the emitted flux. Moreover, the necessity of creating structures thick enough to absorb hard X-rays means that the open channels in the grating are much longer in the X-ray propagation direction than in the transverse one, resulting in angular filtration of the emitted photons. This results in an intensity drop at the sides of the irradiation field, which was at least partly solved through the introduction of curved gratings [182]. An additional factor of flux loss is absorption in the silicon substrates in which the gratings are realized. These are typically several hundred microns thick, which has to be multiplied times three to account for the three gratings present in the setup. Significantly, this is in adverse relation with another limiting factor of grating interferometry, *i.e.* the small available fields of view (currently limited to a maximum of 10 cm [183]). In fact, the realization of gratings of up to 10 cm in side requires the use of at least 6-inch silicon wafers, which are typically 675 μm thick [184]; while thinning is in principle possible, it would rapidly affect robustness for relatively large gratings. These beam losses directly affect exposure times, while the fact that two of the gratings are positioned downstream of the sample affects the delivered dose. Indeed, doses of tens of Grays and exposure times of tens of hours are often encountered for CT applications [185, 186]. While planar imaging applications like mammography are less severely affected by these factors, at the time of writing the best result on mammography specimens were obtained by Stampanoni *et al.* [187], in a study in which doses about 10-20 times higher than in conventional mammography were delivered. Finally, an additional limitation is stability. Gratings have pitches of a few microns, and the method requires phase stepping procedures typically consisting of about 8 steps: the need for at least a 10% accuracy on an individual phase step of a few hundred nanometers results in stability requirements of the order of a few tens of nanometers [188], difficult to realize in clinical cases; in fact, it has been reported that, also in pre-clinical applications, scans have to be regularly interrupted to allow for system re-alignment [185].

Laboratory-based edge illumination XPCi (in what is sometimes referred to as the "coded aperture" approach) seems to be less affected by these issues: following preliminary indications that low doses might be achievable obtained during a proof-of-concept cartilage study [116], this was more thoroughly demonstrated in a dedicated breast study [119], in which doses were independently measured with termoluminescent dosimeters and ionization chambers and cross-checked. More recently, it was demonstrated that also extensions to dark field imaging [111], breast tomosynthesis [189] and CT [190] can be obtained at acceptable dose levels (the latter so far only for pre-clinical applications).

This is due to the much larger pitch of the masks, which enables their fabrication on low X-ray absorbing graphite substrates [191], and in particular to the fact that one of the two masks is placed upstream of the sample, thus protecting it from unwanted dose delivery. With reference to fig. 14, it can be noticed that the only source of "extra" dose with respect to a standard configuration in which no optical elements are used is the portion of each beamlet impinging on the solid septa of the detector mask. As discussed in detail in ref. [119], this portion can be made almost arbitrarily small, hence making the method practically 100% dose efficient.

For the same reason, plus the fact that a source grating is not needed, exposure times are also less affected than in GI, and in fact some of the breast images presented in [119] were acquired in a matter of a few seconds, which begins to be compatible with clinical requirements, despite the suboptimal nature of the used prototype. Work is currently underway to demonstrate that this concept can be extended to CT, and allow for example a full 3D scan of a small animal in a few minutes.

The use of large mask pitches has at least two additional advantages, namely scalability to large fields of view (due to low aspect ratio and consequent use of less demanding micro-fabrication methods), and much reduced stability requirements. Indeed most EI experiments at UCL were conducted in a room on the second floor of a populated building, which constantly "shakes" by about 2-3 μm. So long as the "standard" EI systems were used, which have a maximum resolution of about 20 μm [116], these vibrations did not seem to affect image quality, and in fact images reported *e.g.* in papers [88,104,110,111,116,119] were obtained without any anti-vibration measure in place. This resilience of the method to environmental vibrations was observed already when the first prototype was built and tested [100]. Indeed, problems due to these vibrations were not observed until microscopic approaches were developed; however, also in that case, simple isolation through air cushions was sufficient to solve the problem, and obtain a resolution of the order of 1 μm [192]. Moreover, it has been recently demonstrated that the system can be kept dynamically aligned through a feedback mechanism [107], based on the fact that the detector output is in itself an indication of the masks' position. Importantly, the larger mask pitch that enables the above advantages has no reverse effect on the phase sensitivity [110, 193], and indeed the simultaneous implementation of low-dose and high sensitivity has been recently discussed [194].

However, it is in principle possible that, since the Talbot effect is not exploited, longer sample-to-detector distances might be required by EI compared to grating approaches. Considering also that in EI the projected source size needs to be smaller than the inter-beamlet separation, this might lead to overall less compact setups, and is currently the subject of investigation. On a related note, the current need to use source sizes not larger than 100 μm can make the system relatively expensive, since specialized high-powered sources might be required; moreover, in terms of clinical translation, at the moment these sources are only available in the area of mammography. Strategies to enable the use of larger source sizes are therefore also under investigation.

5. – Conclusions

Research carried out in the last twenty years has demonstrated beyond doubt that XPCi can radically transform diagnostic radiology and many other fields —practically any area in which X-rays are used. Specifically on this aspect, it is important to notice that the use of X-rays in science and society, although sometimes overlooked, is all-pervasive: a partial list of areas of application would include biology, material science, non-destructive testing, security scans, paleonthology and cultural heritage in general, and many others.

In medicine, transition to XPCi would lead to earlier diagnosis and consequently to a reduction of the mortality rate; as well as for diagnosis, X-ray imaging is extensively used in treatment planning, assessment, delivery and follow-up. In the authors' opinion, the Trieste *in vivo* experience on human patients is particularly significant, and provides the ultimate demonstration, in case one was needed, that XPCi can indeed make a significant difference.

Some technological hurdles remain to be overcome to make this happen. Free-space propagation has been particularly attractive for its simplicity: indeed, the Trieste study is based on it, and it cannot be denied that a method not requiring any optical element has significant advantages. However, the current state of the art of X-ray sources does

not seem to allow its clinical implementation: if the source size is sufficiently small as to produce significant free-space propagation-induced phase enhancements, the exposure time is too long for clinical applications; conversely, if the source is made sufficiently large as to allow clinically acceptable exposure times, phase-induced image benefits practically disappear. Hence, the clinical translation of free-space propagation XPCi seems to depend on the development of innovative X-ray source technologies, an area bubbling with extremely promising research ideas, but in which an ultimate solution does not seem to have been identified yet.

This shifts the balance (at least for the time being) on methods that can work with conventional, extended and incoherent, sources. With the caveat of an excessively large projected source size reversely affecting image resolution, grating interferometry provides access to larger (and therefore cheaper and potentially more powerful) focal spots than edge illumination. However, the emitted flux is highly suppressed by the two absorption gratings (one of which has an open fraction typically smaller than 50%), and by attenuation in the three silicon substrates. As discussed above, this has also severe consequences on the efficiency of the dose delivery. Moreover, significant hurdles need to be overcome in terms of mechanical stability and dimensions of the field of view —although interesting proposals exist to overcome the latter by means of scanning approaches [195].

Edge illumination seems to have at least partially solved the problems of excessive dose and exposure time, and has significantly relaxed the stability requirements; moreover, large aperture masks can already be fabricated. However at the moment it allows the use of source sizes up to 100 μm. Sources of this size that can produce sufficient fluxes already exist and are used in *e.g.* mammography, but are typically at the high-end of the technology and consequently quite expensive. Moreover, most system used so far are 2 m long; a 1.5 m system has been designed [99] and is currently under construction, and investigations are underway to understand whether it will be possible in the future to realize even more compact systems.

As a final consideration, it should be noted that the final developments needed to translate these approaches into clinical practice fall into a sort of intermediate, "grey area" of funding scenarios. The more "translational" aspects are not considered to be basic science anymore, and yet, at least in the current economic climate, companies tend to find them too risky to undertake them in full. As a consequence, they have a tendency to leave the "de-risking" business with the researchers, who however might struggle to find appropriate funding tools through the usual channels of Research Councils, etc. It would therefore look like a more "adventurous" attitude on the companies' side (especially the big ones, which are active in the medical area and which could muster the appropriate resources) could be a necessary requisite to reach the final goal of translating the full potential of XPCi into the clinics and beyond.

* * *

A. Olivo's work on X-ray phase has been and is primarily supported by the UK Engineering and Physical Sciences Research Council (EPSRC), grants EP/G004250/1; EP/I022562/1; EP/I021884/1 and EP/L001381/1. E. Castelli would like to kindly thank all present and past members of the SYRMEP collaboration: while naming them individually would be too long for an acknowledgments section, a partial but representative list can be obtained from refs. [34] and [149].

Appendix A.

2×2 contingency table

A 2×2 contingency table can be used in order to evaluate a clinical diagnostic test. It is in fact possible to verify the test efficiency if the presence or absence of the disease is known in a sample of patients undergoing the diagnostic test [196,197]. The definition of various quantities is shown in table IV.

With reference to table IV contents, the quantities listed in table V can be defined.

Two interesting cases are considered in tables VI and VII, the Ideal test and (two examples of the) the Null test, respectively. Pertinent numerical examples are discussed, in particular with respect to the field of mammographic tests: the sample is of a total of 10,000 patients and the prevalence is of 1%, which is a reasonable value in this area.

In the case of the Ideal test, a top-level efficiency is considered: the false positives and false negatives are zero; therefore sensitivity, specificity and PPV are all equal to 100%. Hence the test can be considered "perfect": it finds no false positives and at the same time misses no one with the disease. The ideal situation is of course hardly ever encountered in practice, but the Ideal test case can nevertheless be useful in discussions on the results of the clinical experimentation (see *e.g.* end of sect. **3**˙4).

In the second case (Null test), a minimum of efficiency is considered; in the two cases, the sample is divided in a different number of test positives and test negatives, but the percentage of ill patients is the same in the two cases and is equal to the prevalence; *i.e.* the PPV is equal to the prevalence. Of course the aim of any diagnostic test is to improve the PPV with respect to the prevalence: a mere proportionality makes the test completely useless, which applies in the same way to both cases represented in table VII.

The two parts of table VIII enable discussing a more realistic numerical simulation. In sect. **3**˙2, the diagnostic performance of mammography is reported to have sensitivity between 60% and 90%, and specificity between 80% and 95%. If maximum values are assumed for both these quantities, the Data 2×2 contingency table with the corresponding Null test can be computed. This results in a PPV of 15.4%: out of 6.5 test positives, only 1 patient is really ill. As far as the null test is concerned, the corresponding sensitivity would have to be equal to 5.85%, much lower than the 90% sensitivity of the data.

The next step in the verification of the test's effectiveness consists in checking whether

Table IV. – 2×2 *contingency table.*

	Disease		
Test	True Positive	False Positive	Test Positive
	False Negative	True Negative	Test Negative
	Disease Positive (ill)	Disease Negative (healthy)	Total

Table V. – *Prevalence, sensitivity, specificity and positive predictive value (PPV) defined as a function of the contingency table's entries.*

Prevalence	Ill / Total
Sensitivity	True Positives / Ill
Specificity	True Negatives / Healthy
Positive Predictive Value (PPV)	True Positives / Test Positives

TABLE VI. – 2×2 *contingency table of an Ideal test.*

True positive: 100	False positive: 0	Test positive: 100
False negative: 0	True Negative: 9900	Test negative: 9900
Ill: 100	Healthy: 9900	Total: 10000

TABLE VII. – 2×2 *contingency tables for two examples of "Null" test.*

Null test – case 1				Null test – case 2		
True positive: 1	False positive: 99	Test positive: 100		True positive: 10	False positive: 990	Test positive: 1000
False negative: 99	True Negative: 9801	Test negative: 9900		False negative: 90	True Negative: 8910	Test negative: 9000
Ill: 100	Healthy: 9900	Total: 10000		Ill: 100	Healthy: 9900	Total: 10000

TABLE VIII. – 2×2 *contingency tables for a realistic example (corresponding to prevalence = 1%, sensitivity = 90%, specificity = 95% and PPV = 15%) and relative null test.*

Data:				Null test:		
True positive: 90	False positive: 495	Test positive: 585		True positive: 5.85	False positive: 579.15	Test positive: 585
False negative: 10	True Negative: 9405	Test negative: 9415		False negative: 94.15	True Negative: 9320.85	Test negative: 9415
Ill: 100	Healthy: 9900	Total: 10000		Ill: 100	Healthy: 9900	Total: 10000

the data test is compatible (within a given level of confidence) with the corresponding null test. The computation of the Pearson Chi-square [198] with the appropriate probability, or, in particular cases, the Two-tailed Fisher exact probability, provides this type of answer. The results of this procedure have been used for the table of "Comparison of diagnostic performances" presented in sect. **3**˙4.

The total number of patients for this clinical research is 69, which allows computing the Two-tailed Fisher exact probability. For the conventional digital mammography this value is 0.012, while for the phase contrast mammography with synchrotron radiation it is lower than 0.000001: this demonstrates the superiority of the second test, by taking into account directly the compatibility with the corresponding null test.

Also without resorting to statistical calculations, it is possible to become convinced that phase contrast mammography with synchrotron radiation performs better simply by looking at the values of the PPV in the two cases. In fact, the PPV goes from 55% to 93%, with a common prevalence of 42%. The PPV is a ratio: in the examined case, the numerator is practically constant, but the denominator decreases substantially. As has been already pointed out, while there was no increase in true positives, a substantial decrease of false positives was observed, with a corresponding increase, in this particular case, of true negatives.

REFERENCES

[1] Brailsford J. F., *Br. J. Radiol.*, **19** (1946) 453.
[2] Mould R. F., *A History of X-rays and radium* (IPC Business Press Ltd, London, UK) 1980.
[3] Hounsfield G. N., *Br. J. Radiol.*, **46** (1973) 1016.
[4] Ambrose J., *Br. J. Radiol.*, **46** (1973) 1023.
[5] Yaffe M. J. and Rowlands J. A., *Med. Phys.*, **42** (1997) 1.
[6] Johns H. E. and Cunningham J. R., *The Physics of Radiology*, 4th edition (Charles C. Thomas Pub. Ltd, Sprinfield, IL, USA) 1983.
[7] Webb S., *The Physics of Medical Imaging* (IOP Publishing, Bristol, UK) 1988.
[8] Suortti P. and Thomlinson W., *Phys. Med. Biol.*, **48** (2003) R1.
[9] Bravin A., Coan P. and Suortti P., *Phys. Med. Biol.*, **58** (2013) R1.
[10] Bonse U. and Hart M., *Appl. Phys. Lett.*, **6** (1965) 155.
[11] Snigirev A., Snigireva I., Kohn V., Kuznetsov S. and Schelokov I., *Rev. Sci. Instrum.*, **66** (1995) 5486.
[12] Wilkins S. W., Gureyev T. E., Gao D., Pogany A. and Stevenson A. W., *Nature*, **384** (1996) 335.
[13] Davis T. J., Gao D., Gureyev T. E., Stevenson A. W. and Wilkins S. W., *Nature*, **373** (1995) 595.
[14] Ingal V. N. and Beliaevskaya E. A., *J. Phys. D: Appl. Phys.*, **28** (1995) 2314.
[15] Olivo A., Arfelli F., Cantatore G., Longo R., Menk R. H., Pani S., Prest M., Poropat P., Rigon L., Tromba G., Vallazza E. and Castelli E., *Med. Phys.*, **28** (2001) 1610.
[16] Bettini A., *Le onde e la luce* (Zanichelli, Bologna, Italy) 1993.
[17] Peterzol A., Olivo A., Rigon L., Pani S. and Dreossi D., *Med. Phys.*, **32** (2005) 3617.
[18] Munro P. R. T., Ignatyev K., Speller R. D. and Olivo A., *Opt. Express*, **18** (2010) 4103.
[19] Bonse U. and Hart M., *Appl. Phys. Lett.*, **7** (1965) 99.
[20] Bruning J. H., Herriot D. R., Gallagher J. E., Rosenfeld D. P., White A. D. and Brangaccio D. J., *Appl. Opt.*, **13** (1974) 2693.
[21] Ando M. and Hosoya S., in *Proceedings of the 6th International Conference on X-Ray Optics and Microanalysis* (University of Tokyo Press, 1972) pp. 63-68.
[22] Hart M., *Proc. R. Soc. A*, **346** (1975) 1.
[23] Momose A., *Nucl. Instrum. Methods A*, **352** (1995) 622.
[24] Takeda T., Momose A., Itai Y., Wu J. and Hirano K., *Acad. Radiol.*, **2** (1995) 799.
[25] Momose A., Takeda T., Itai Y. and Hirano K., *Nat. Med.*, **2** (1996) 473.
[26] Momose A. and Fukuda J., *Med. Phys.*, **22** (1995) 375.
[27] Momose A., Takeda T. and Itai Y., *Acad. Radiol.*, **2** (1995) 883.
[28] Wen H., Gomella A. A., Patel A., Lynch S. K., Morgan N. Y., Anderson S. A., Bennett E. E., Xiao X., Liu C. and Wolfe D. E., *Nat. Commun.*, **4** (2013) 2659.
[29] Ando M., Sugiyama H., Zhang X., Hyodo K., Maksimenko A. and Pattanasiriwisawa W., *Jpn. J. Appl. Phys.*, **40** (2001) L298.
[30] Ando M., Hyodo K., Sugiyama H., Maksimenko A., Pattanasiriwisawa W., Mori K., Robertson J., Rubenstein E., Tanaka Y., Chen J. Y., Xian D. C. and Zhang X. W., *Jpn. J. Appl. Phys.*, **41** (2002) 4742.
[31] Maksimenko A., Ando M., Sugiyama H., Pattanasiriwisawa W. and Hyodo K., *Jpn. J. Appl. Phys.*, **42** (2003) L1096.
[32] Wilkins S. W., *Improved X-ray optics, especially for phase contrast imaging*, International Patent **WO 95/05725** (23 Feb 1995).
[33] Azarov L. V., *Elements of X-ray crystallography* (Mc Graw-Hill, New York) 1968.

[34] Arfelli F., Bonvicini V., Bravin A., Cantatore G., Castelli E., Dalla Palma L., Di Michiel M., Fabrizioli M., Longo R., Menk R. H., Olivo A., Pani S., Pontoni D., Poropat P., Prest M., Rashevsky A., Ratti M., Rigon L., Tromba G., Vacchi A., Vallazza E. and Zanconati F., *Radiology*, **215** (2000) 286.
[35] Chapman D., Thomlinson W., Johnston R. E., Washburn D., Pisano E., Gmür N., Zhong Z., Menk R., Arfelli F. and Sayers D., *Phys. Med. Biol.*, **42** (1997) 2015.
[36] Förster E., Goetz K. and Zaumseil P., *Krist. Tech.*, **15** (1980) 937.
[37] Podurets K. M., Somenkov V. A. and Shil'shtein S. S., *Sov. Phys. Tech. Phys.*, **34** (1989) 654.
[38] Ingal V. N., Belyaevskaya E. A. and Efanov V. N., *Method for obtaining the internal structure image of object*, International Patent **WO/021016** (26 Nov 1992).
[39] Dilmanian F. A., Zhong Z., Ren B., Wu X. Y., Chapman L. D., Orion I. and Thomlinson W., *Phys. Med. Biol.*, **45** (2000) 933.
[40] Maksimenko A., Ando M., Hiroshi S. and Yuasa T., *Appl. Phys. Lett.*, **86** (2005) 124105.
[41] Zhu P. P., Wang J. Y., Yuan Q. X., Huang W. X., Shu H., Gao B., Hu T. D. and Wu Z. Y., *Appl. Phys. Lett.*, **87** (2005) 264101.
[42] Huang Z. F., Kang K. J., Li Z., Zhu P. P., Yuan Q. X., Huang W. X., Wang J. Y., Zhang D. and Yu A. M., *Appl. Phys. Lett.*, **89** (2006) 041124.
[43] Nesterets Y. I., Gureyev T. E. and Wilkins S. W., *Appl. Phys. Lett.*, **89** (2006) 264103.
[44] Rigon L., Besch H. J., Arfelli F., Menk R. H., Heitner G. and Plothow-Besch H., *J. Phys. D: Appl. Phys.*, **36** (2003) A107.
[45] Pagot E., Cloetens P., Fiedler S., Bravin A., Coan P., Baruchel J., Hartwig J. and Thomlinson W., *Appl. Phys. Lett.*, **82** (2003) 3421.
[46] Oltulu O., Zhong Z., Hasnah M., Wernick M. N. and Chapman D., *J. Phys. D: Appl. Phys.*, **36** (2003) 2152.
[47] Rigon L., Astolfo A., Arfelli F. and Menk R. H., *Eur. J. Radiol.*, **68** (2008) S3.
[48] Sunaguchi N., Yuasa T., Huo Q., Ichihara S. and Ando M., *Appl. Phys. Lett.*, **97** (2010) 153701.
[49] Pisano E. D., Johnston R. E., Chapman D., Geradts J., Iacocca M. V., Livasy C. A., Washburn D. B., Sayers D. E., Zhong Z., Kiss M. F. and Thomlinson W. C., *Radiology*, **214** (2000) 895.
[50] Keyriläinen J., Fernandez M., Karjalainen-Lindsberg M.-L., Virkkunen P., Leidenius M., Von Smitten K., Sipilä P., Fiedler S., Suhonen H., Suortti P. and Bravin A., *Radiology*, **249** (2008) 321.
[51] Zhao Y., Brun E., Coan P., Huang Z., Sztrókay A., Diemoz P. C., Liebhardt S., Mittone A., Gasilov S., Miao J. and Bravin A., *Proc. Natl. Acad. Sci. U.S.A.*, **109** (2012) 18290.
[52] Mollenhauer J., Aurich M. E., Zhong Z., Muehlman C., Cole A. A., Hasnah M., Oltulu O., Kuettner K. E., Margulis A. and Chapman L. D., *Osteoarthr. Cartil.*, **10** (2002) 163.
[53] Coan P., Wagner A., Bravin A., Diemoz P. C., Keyriläinen J. and Mollenhauer J., *Phys. Med. Biol.*, **55** (2010) 7649.
[54] Connor D. M., Sayers D., Sumner D. R. and Zhong Z., *Phys. Med. Biol.*, **51** (2006) 3283.
[55] Kitchen M. J., Lewis R. A., Yagi N., Uesugi K., Paganin D., Hooper S. B., Adams G., Jureczek S., Singh J., Christensen C. R., Hufton A. P., Hall C. J., Cheung K. C. and Pavlov K. M., *Br. J. Radiol.*, **78** (2005) 1018.
[56] Born M. and Wolf E., *Principles of Optics*, 6th edition. (Pergamon Press, Oxford, UK) 1980.
[57] Arfelli F., Assante M., Bonvicini V., Bravin A., Cantatore G., Castelli E., Dalla Palma L., Di Michiel M., Longo R., Olivo A., Pani S., Pontoni D., Poropat P., Prest M., Rashevsky A., Tromba G., Vacchi A., Vallazza E. and Zanconati F., *Phys. Med. Biol.*, **43** (1998) 2845.

[58] Pogany A., Gao D. and Wilkins S. W., *Rev. Sci. Instrum.*, **68** (1997) 2774.
[59] Olivo A., *Nucl. Instrum. Methods A*, **548** (2005) 194.
[60] Olivo A. and Speller R., *Phys. Med. Biol.*, **51** (2006) 2015.
[61] Olivo A. and Speller R. D., *Phys. Med. Biol.*, **54** (2009) N347.
[62] De Caro L., Scattarella F., Tangaro S., Pelliccia D., Giannini C., Bottigli U. and Bellotti R., *Med. Phys.*, **38** (2011) 1951.
[63] Hwu Y., Hsieh H., Lu M. J., Tsai W. L., Lin H. M., Goh W. C., Lai B., Je J. H., Kim C. K., Noh D. Y., Youn H. S., Tromba G. and Margaritondo G., *J. Appl. Phys.*, **86** (1999) 4613.
[64] Diemoz P. C., Endrizzi M., Zapata C. E., Pesic Z. D., Rau C., Bravin A., Robinson I. K. and Olivo A., *Phys. Rev. Lett.*, **110** (2013) 138105.
[65] Suzuki K. and Haig I., *Phil. Trans. R. Soc. A*, **372** (2014) 20130036.
[66] Nesterets Y. I., Gureyev T. E. and Wilkins S. W., *J. Phys. D: Appl. Phys.*, **38** (2005) 4259.
[67] Gureyev T. E., Mayo S., Wilkins S. W., Paganin D. and Stevenson A. W., *Phys. Rev. Lett.*, **86** (2001) 5827.
[68] Gureyev T. E., Nesterets Y. I., Stevenson A. W., Miller P. R., Pogany A. and Wilkins S. W., *Opt. Express*, **16** (2008) 3223.
[69] Gureyev T. E., Mayo S., Myers D. E., Nesterets Y. I., Paganin D., Pogany A., Stevenson A. W. and Wilkins S. W., *J. Appl. Phys.*, **105** (2009) 102005.
[70] Nesterets Y. I., Wilkins S. W., Gureyev T. E., Pogany A. and Stevenson A. W., *Rev. Sci. Instrum.*, **76** (2005) 093706.
[71] Nugent K. A., Gureyev T. E., Cookson D. F., Paganin D. and Barnea Z., *Phys. Rev. Lett.*, **77** (1996) 2961.
[72] Gureyev T. E. and Wilkins S. W., *J. Opt. Soc. Am. A*, **15** (1998) 579.
[73] Cloetens P., Ludwig W. Baruchel J., Van Dyck D., Van Landuyt J., Guigay J. P. and Schlenker M., *Appl. Phys. Lett.*, **75** (1999) 2912.
[74] Paganin D., Mayo S., Gureyev T. E., Miller P. R. and Wilkins S. W., *J. Microsc.*, **206** (2002) 22.
[75] Cloetens P., Pateyron-Salomé M., Buffière J. Y., Peix G., Baruchel J., Peyrin F. and Schlenker M., *J. Appl. Phys.*, **81** (1997) 5878.
[76] Buffière J. Y., Maire E., Cloetens P., Lormand G. and Fougères R., *Acta Mater.*, **47** (1999) 1613.
[77] Spanne P., Raven C., Snigireva I. and Snigirev A., *Phys. Med. Biol.*, **44** (1999) 741.
[78] Bronnikov A. V., *Opt. Commun.*, **171** (1999) 239.
[79] Barty A., Nugent K. A., Roberts A. and Paganin D., *Opt. Commun.*, **175** (2000) 329.
[80] Stevenson A. W., Gureyev T. E., Paganin D., Wilkins S. W., Weitkamp T., Snigirev A., Rau C., Snigireva I., Youn H. S., Dolbnya I. P., Yun W., Lai B., Garrett R. F., Cookson D. F., Hyodo K. and Ando M., *Nucl. Instrum. Methods B*, **199** (2003) 427.
[81] Lewis R., *Phys. Med. Biol.*, **49** (2004) 3573.
[82] Zhou S. A. and Brahme A., *Phys. Medica*, **24** (2008) 129.
[83] Olivo A., *Rec. Pat. Biomed. Eng.*, **3** (2010) 95.
[84] Mayo S. C., Stevenson A. W. and Wilkins S. W., *Materials*, **5** (2012) 937.
[85] Di Michiel M., Olivo A., Tromba G., Arfelli F., Bonvicini V., Bravin A., Cantatore G., Castelli E., Dalla Palma L., Longo R., Pani S., Pontoni D., Poropat P., Prest M., Rashevsky A., Vacchi A. and Vallazza E., in *Medical Applications of Synchrotron Radiation*, edited by Ando M. and Uyama C. (Springer-Verlag, Tokyo) 1998, pp. 78-82.
[86] Munro P. R. T., Hagen C. K., Szafraniec M. B. and Olivo A., *Opt. Express*, **21** (2013) 11187.
[87] Olivo A. and Speller R., *Phys. Med. Biol.*, **53** (2008) 6461.

[88] Munro P. R. T., Ignatyev K., Diemoz P. C., Szafraniec M. B., Hagen C. K., Millard T. P, Zapata C. E., Speller R. D. and Olivo A., *AIP Conf. Proc.*, **1466** (2012) 118.
[89] Olivo A., Arfelli F., Dreossi D., Longo R., Menk R. H., Pani S., Poropat P., Rigon L., Zanconati F. and Castelli E., *Phys. Med. Biol.*, **47** (2002) 469.
[90] Arfelli F., Bonvicini V., Bravin A., Cantatore G., Castelli E., Dalla Palma L., Di Michiel M., Fabrizioli M., Longo R., Olivo A., Pani S., Pontoni D., Poropat P., Prest M., Rashevsky A., Rigon L., Tromba G., Vacchi A. and Vallazza E., *Inform. MIDEM*, **1** (1999) 26.
[91] Cabrini S., Perennes F., Marmiroli B., Olivo A., Carpentiero A., Kumar R., Candeloro P. and Di Fabrizio E., *Microsyst. Technol.*, **11** (2005) 370.
[92] Olivo A., Pani S., Dreossi D., Montanari F., Bergamaschi A., Vallazza E., Arfelli F., Longo R., Rigon L. and Castelli E., *Rev. Sci. Instrum.*, **74** (2003) 3460.
[93] Olivo A., Arfelli F., Bergamaschi A., Longo R., Menk R. H., Montanari F., Pani S., Poropat P., Rigon L., Vallazza E. and Castelli E., in *IWDM 2002: Proceedings of the 6th International Workshop on Digital Mammography*, edited by Peitgen H. O. (Springer, Berlin) 2003, pp. 48-50.
[94] Munro P. R. T., Rigon L., Ignatyev K., Lopez F. C. M., Dreossi D., Speller R. D. and Olivo A., *Opt. Exp.*, **21** (2013) 647.
[95] Olivo A, Diemoz P. C. and Bravin A., *Opt. Lett.*, **37** (2012) 915.
[96] Diemoz P. C., Endrizzi M., Zapata C. E., Bravin A., Speller R. D., Robinson I. K. and Olivo A., *J. Instrum.*, **8** (2013) C06002.
[97] Diemoz P. C., Endrizzi M., Bravin A., Robinson I. K. and Olivo A., *Phil. Trans. R. Soc. A*, **372** (2014) 20130128.
[98] Olivo A. and Speller R., *Appl. Phys. Lett.*, **91** (2007) 074106.
[99] Olivo A. and Speller R., *Phys. Med. Biol.*, **52** (2007) 6555.
[100] Olivo A., Ignatyev K., Munro P. R. T. and Speller R., *Appl. Opt.*, **50** (2011) 1765.
[101] Ignatyev K., Munro P. R. T., Chana D., Speller R. and Olivo A., *J. Appl. Phys.*, **110** (2011) 014906.
[102] Munro P. R. T., Ignatyev K., Speller R. D. and Olivo A., *Opt. Express*, **18** (2010) 19681.
[103] Munro P. R. T. and Olivo A., *Phys. Rev. A*, **87** (2013) 053838.
[104] Munro P. R. T., Ignatyev K., Speller R. D. and Olivo A., *Proc. Natl. Acad. Sci. U.S.A.*, **109** (2012) 13922.
[105] Munro P. R. T., Endrizzi M, Diemoz P. C., Hagen C. K., Szafraniec M. B., Millard T. P., Zapata C. E., Speller R. D. and Olivo A., *Phil. Trans. R. Soc. A*, **372** (2014) 20130029.
[106] Ignatyev K., Munro P. R. T., Speller R. and Olivo A., *Rev. Sci. Instrum.*, **82** (2011) 073702.
[107] Millard T. P, Endrizzi M., Ignatyev K., Hagen C. K., Munro P. R. T., Speller R. and Olivo A., *Rev. Sci. Instrum.*, **84** (2013) 083702.
[108] Olivo A., Ignatyev K., Munro P. R. T. and Speller R., *Nucl. Instrum. Methods A*, **648** (2011) S28.
[109] Olivo A., Bohndiek S. E., Griffiths J. A., Konstantinidis A. and Speller R., *Appl. Phys. Lett.*, **94** (2009) 044108.
[110] Diemoz P. C., Hagen C. K., Endrizzi M. and Olivo A., *Appl. Phys. Lett.*, **103** (2013) 244104.
[111] Endrizzi M., Diemoz P. C., Millard T. P., Jones J. L., Speller R. D., Robinson I. K. and Olivo A., *Appl. Phys. Lett.*, **104** (2014) 024106.
[112] Endrizzi M., Diemoz P. C., Munro P. R. T, Hagen C. K., Szafraniec M. B., Millard T. P., Zapata C. E., Speller R. D. and Olivo A., *J. Instrum.*, **8** (2013) C05008.
[113] Olivo A., Chana D. and Speller R., *J. Phys. D: Appl. Phys.*, **41** (2008) 225503.
[114] Olivo A., Ignatyev K., Munro P. R. T. and Speller R., *Nucl. Instrum. Methods A*, **610** (2009) 604.

[115] Ignatyev K., Munro P. R. T., Speller R. and Olivo A., *Materials*, **4** (2011) 1846.
[116] Marenzana M., Hagen C. K., Das Neves Borges P., Endrizzi M., Szafraniec M. B., ignatyev K. and Olivo A., *Phys. Med. Biol.*, **57** (2012) 8173.
[117] Marenzana M., Hagen C. K., Das Neves Borges P., Endrizzi M., Szafraniec M. B., Vincent T. L., Rigon L., Arfelli F., Menk R. H. and Olivo A., *Philos. Trans. R. Soc. A*, **372** (2014) 20130127.
[118] Kavanagh A., Olivo A., Speller R. and Vojnovic B., *Biomed. Opt. Express*, **5** (2014) 93.
[119] Olivo A., Gkoumas S., Endrizzi M., Hagen C. K., Szafraniec M. B., Diemoz P. C., Munro P. R. T., Ignatyev K., Johnson B., Horrocks J. A., Vinnicombe S. J., Jones J. L. and Speller R. D., *Med. Phys.*, **40** (2013) 090701.
[120] Endrizzi M., Diemoz P. C., Szafraniec M. B., Hagen C. K., Millard T. P., Zapata C. E., Munro P. R. T, Ignatyev K., Marenzana M., Speller R. D. and Olivo A., *Proc. SPIE*, **8668** (2013) 866812.
[121] Talbot H. F., *Philos. Mag.*, **9** (1836) 401.
[122] Cloetens P, Guigay J. P., De Martino C., Baruchel J. and Schlenker M., *Opt. Lett.*, **22** (1997) 1059.
[123] Cloetens P, Guigay J. P., De Martino C., Salomé M., Schlenker M. and Van Dyck D., *Proc. SPIE*, **3154** (1997) 72.
[124] David C., Nohammer B., Solak H. H. and Ziegler E., *Appl. Phys. Lett.*, **81** (2002) 3287.
[125] Momose A., Kawamoto S., Hamaishi Y., Takai K. and Suzuki Y., *Jpn. J. Appl. Phys.*, **42** (2003) L866.
[126] Weitkamp T., Diaz A., David C., Pfeiffer F., Stampanoni M., Cloetens P. and Ziegler E., *Opt. Express*, **13** (2005) 6296.
[127] Pfeiffer F., Weitkamp T., Bunk O. and David C., *Nat. Phys.*, **2** (2006) 258.
[128] Case W. B., Tomandl M., Dechapunya S. and Arndt M., *Opt. Express*, **17** (2009) 20966.
[129] Pfeiffer F., Weitkamp T., Bunk O. and David C., *Phys. Rev. Lett.*, **98** (2007) 108105.
[130] Pfeiffer F., Bech M., Bunk O., Kraft P., Eikenberry E. F., Brönniman CH., Grünzweig C. and David C., *Nat. Mater.*, **7** (2008) 134.
[131] Zanette I., Weitkamp T., Donath T., Rutishauser S. and David C., *Phys. Rev. Lett.*, **105** (2010) 248102.
[132] Sato G., Kondoh T., Itoh H., Handa S., Yamaguchi K., Nakamura T., Nagai K., Ouchi C., Teshima T., Setomoto Y. and Den T., *Opt. Lett.*, **36** (2011) 3551.
[133] Zanette I., Bech M., Pfeiffer F. and Weitkamp T., *Appl. Phys. Lett.*, **98** (2011) 094101.
[134] Yashiro W., Harasse S., Kawabata K., Kuwabara H., Yamazaki T. and Momose A., *Phys. Rev. B*, **84** (2011) 094106.
[135] Pfeiffer F., Herzen J., Willner M., Chabior M., Auwerer S., Reiser M. and Bamberg F., *Z. Med. Phys.*, **23** (2013) 176.
[136] Wen H., Bennett E. E., Hegedus M. M. and Carroll S. C., *IEEE Trans. Med. Imag.*, **27** (2008) 997.
[137] Wen H., Bennett E. E., Kopace R., Stein A. F. and Pai V., *Opt. Lett.*, **35** (2010) 1932.
[138] Wen H., Bennett E. E., Hegedus M. M. and Rapacchi S., *Radiology*, **251** (2009) 910.
[139] Huang Z. F., Kang K. J., Zhang L., Chen Z. Q., Ding F., Wang Z. T. and Fang Q. G., *Phys. Rev. A*, **79** (2009) 013815.
[140] Choi J. and Park Y. S., *Appl. Phys. Express*, **5** (2012) 042503.
[141] Pelliccia D. and Paganin D. M., *Opt. Express*, **21** (2013) 9308.
[142] Nesterets Y. I. and Wilkins S. W., *Opt. Express*, **16** (2008) 5849.
[143] Morgan K. S., Paganin D. M. and Siu K. K. W., *Opt. Express*, **19** (2011) 19781.

[144] Morgan K. S., Paganin D. M. and Siu K. K. W., *Appl. Phys. Lett.*, **100** (2012) 124102.
[145] Dalla Palma L. and Castelli E., *Proceedings of the workshop on "Scientific and technological application of synchrotron radiation"* (ICTP, Trieste, Italy, 1987) p. 98.
[146] Abrami A., Arfelli F., Barroso R. C., Bergamaschi A., Billè F., Bregant P., Brizzi F., Casarin K., Castelli E., Chenda V., Dalla Palma L., Dreossi D., Fava C., Longo R., Mancini L., Menk R. H., Montanari F., Olivo A., Pani S., Pillon A., Quai E., Kaiser S. R., Rigon L., Rokvic T., Tonutti M., Tromba G., Vascotto A., Venanzi C., Zanconati F., Zanetti A. and Zanini F., *Nucl. Instrum. Methods A*, **548** (2005) 221.
[147] Arfelli F., Abrami A., Bregant P., Chenda V., Cova M. A., De Guarrini F., Dreossi D., Longo R., Menk R. H., Quai E., Rokvic T., Tonutti M., Tromba G., Zanconati F. and Castelli E., *AIP Conf. Proc.*, **879** (2007) 1895.
[148] Castelli E., Arfelli F., Dreossi D., Longo R., Rokvic T., Cova M. A., Quaia E., Tonutti M., Zanconati F., Abrami A., Chenda V., Menk R. H., Quai E., Tromba G., Bregant P. and De Guarrini F., *Nucl. Instrum. Methods A*, **572** (2007) 237.
[149] Castelli E., Tonutti M., Arfelli F., Longo R., Quaia E., Rigon L., Sanabor D., Zanconati F., Dreossi D., Abrami A., Quai E., Bregant P., Casarin K., Chenda V., Menk R. H., Rokvic T., Vascotto A., Tromba G. and Cova M. A., *Radiology*, **259** (2011) 684.
[150] Longo R., Tonutti M., Rigon L., Arfelli F., Dreossi D., Quai E., Zanconati F., Castelli E., Tromba G. and Cova M. A., *Phil. Trans. R. Soc. A*, **372** (2014) 20130025.
[151] Vainio H. and Bianchini F. (Editors), *IARC Handbooks of Cancer Prevention, Volume 7: Breast Cancer Screening* (IARC Press, Lyon, France) 2002, p. 30.
[152] Pisano E. D., Gatsonis C., Hendrick E., Yaffe M., Baum J. K., Acharyya S., Conant E. F., Fajardo L. L., Bassett L., D'Orsi C., Jong R. and Rebner M., *New Engl. J. Med.*, **353** (2005) 1773.
[153] Blanks R. G., Moss S. M. and Patnick J., *J. Med. Screen.*, **7** (2000) 195.
[154] Venkatesan A., Chu P., Kerlikowske K., Sickles E. A. and Smith-Bindman R., *Radiology*, **250** (2009) 648.
[155] Karellas A. and Vedantham S., *Med. Phys.*, **35** (2008) 4878.
[156] Lindfors K. K., Boone J. M., Nelson T. R., Yang K., Kwan A. L. C. and Miller D. F., *Radiology*, **246** (2008) 725.
[157] Fitzgerald R., *Phys. Today*, **53** (2000) 23.
[158] Takeda T., Momose A., Ueno E. and Itai Y., *J. Synchrotron Radiat.*, **5** (1998) 1133.
[159] Ingal V. N., Beliaevskaya E. A., Brianskaya A. P. and Merkurieva R. D., *Phys. Med. Biol.*, **43** (1998) 2555.
[160] Bravin A., Keyriläinen J., Fernández M., Fiedler S., Nemoz C., Karjalainen-Lindsberg M. L., Tenhunen M., Virkkunen P., Leidenius M., Von Smitten K., Sipilä P. and Suortti P., *Phys. Med. Biol.*, **52** (2007) 2197.
[161] Kao T., Connor D., Dilmanian F. A., Faulconer L., Liu T., Parham C., Pisano E. D. and Zhong Z., *Phys. Med. Biol.*, **54** (2009) 3247.
[162] Dix W. R., Kupper W., Dill T., Hamm C. W., Job H., Lohmann M., Reime B. and Ventura R., *J. Synchrotron Radiat.*, **10** (2003) 219.
[163] Sarnelli A., Nemoz C., Elleaume H., Estève F., Bertrand B. and Bravin A., *Phys. Med. Biol.*, **50** (2005) 725.
[164] *Breast imaging reporting and data system (BIRADS)*, 4th edition (American College of Radiology, Reston, VA) 2003.
[165] Olivo A. and Robinson I., *Phil. Trans. R. Soc. A*, **372** (2014) 20130359.
[166] Bulyak E., Gladkikh P., Zelinsky A., Karnaukhov I., Kononenko I., Lapshin V., Mytsykov A., Telegin Y., Khodyachikh A., Shcherbakov A., Molodkin V., Nemoshkalenko V. and Shpak A., *Nucl. Instrum. Methods A*, **487** (2002) 241.

[167] Bech M., Bunk O., David D., Ruth R., Rifkin J., Loewen R., Feidenhahsl R. and Pfeiffer F., *J. Synchrotron Radiat.*, **16** (2008) 43.
[168] Oliva P., Bacci A., Bottigli U., Carpinelli M., Delogu P., Ferrario M., Giulietti D., Golosio B., Petrillo V., Serafini L., Tomassini P., Vaccarezza C., Vicario C. and Stefanini A., *Nucl. Instrum. Methods A*, **615** (2010) 93.
[169] Bruni C., Artemiev N., Roux R., Variola A., Zomer F and Loulergue A., in *Proceedings of UVX 2010 - 10e Colloque sur les Sources Coherentes et Incoherentes UV, VUV et X: Applications et Developpements Recents* (EDP Science, Paris) 2011, pp. 49-55.
[170] Krol A., Ikhlef A., Kieffer J. C., Bassano D. A., Chamberlain C. C., Jiang Z., Pepin H. and Prasad S. C., *Med. Phys.*, **24** (1997) 725.
[171] Cipiccia S., Islam M. R., Ersfeld B., Shanks R. P., Brunetti E., Vieux G., Yang X., Issac R. C., Wiggins S. M., Welsh G. H., Anania M.-P., Maneuski D., Montgomery R., Smith G., Hoek M., Hamilton D. J., Lemons N. R. C., Symes D., Rajeev P. P, Shea V. O., Dias J. M. and Jaroszynski D. A., *Nat. Phys.*, **7** (2011) 867.
[172] Popmintchev T., Chen M.-C., Popmintchev D., Arpin P., Brown S., Alisauskas S., Andriukaitis G., Balciunas T., Mücke O. D., Pugzlys A., Baltuska A., Shim B., Schrauth S. E., Gaeta A., Hernandez-Garcia C., Plaja L., Becker A., Jaron-Becker A., Murnane M. M. and Kapteyn H. C., *Science*, **336** (2012) 1287.
[173] Najmudin Z., Kneip S., Bloom M. S., Mangles S. P. D., Chekhlov O., Dangor A. E., Döpp A., Ertel K, Hawkes S. J., Holloway J., Hooker C. J., Jiang J., Lopes N. C., Nakamura H., Norreys P. A., Rajeev P. P., Russo C., Streeter M. J. V., Symes D. R. and Wing M., *Phil. Trans. R. Soc. A*, **372** (2014) 20130032.
[174] Van Heekeren J., Kostenko A., Hanashima T., Yamada H., Stallinga S., Offerman S. E. and Van Vliet L. J., *Med. Phys.*, **38** (2011) 5136.
[175] Larsson D. H., Takman P. A. C., Lundström U., Burvall A. and Hertz H. M., *Rev. Sci. Instrum.*, **82** (2011) 123701.
[176] Larsson D. H., Lundström U., Westermark U., Takman P. A. C., Burvall A., Arsenian Henriksson M. and Hertz H. M., *Proc. SPIE*, **8313** (2012) 83130N.
[177] Morita T., Yamada M., Kano A., Nagatsuka S., Honda C. and Endo T., in: *Lecture Notes in Computer Science* (Springer, Berlin) 2008, pp. 48-54.
[178] Kotre C. J. and Birch I. P., *Phys. Med. Biol.*, **44** (1999) 2853.
[179] Vine D. J., Paganin D. M., Pavlov K. M., Kräusslich L., Wehrhan O., Uschmann I. and Föster E., *Appl. Phys. Lett.*, **91** (2007) 254110.
[180] Connor D. M., Cole E. B., Zhong Z., Parham C. A. and Pisano E. D., *Proc. SPIE*, **8313** (2012) 83134G.
[181] Lanza R., Horn B. and Damato A., *Phase-contrast X-ray imaging*, International Patent **WO 09/058976** (7 May 2009).
[182] Revol V., Kottler C., Kaufmann R., Jerjen I., Lüthi T., Cardot F., Niedermann P., Straumann U., Sennhauser U. and Urban C., *Nucl. Instrum. Methods A*, **648** (2011) S302.
[183] Baborowski J., Revol V., Kottler C., Kaufmann R., Niedermann P., Cardot F., Dommann A., Neels A. and Despont M., in *Proceedings of the 27th IEEE International Conference on Micro Electro Mechanical Systems* (2014), pp. 490-3.
[184] Goldstein M. and Watanabe M., *ECS Trans.*, **16** (2008) 3.
[185] Tapfer A., Bech M., Velroyen A., Meiser J., Mohr J., Walter M., Schulz J., Pauwels B., Bruyndonckx P., Liu X., Sasov A. and Pfeiffer F., *Proc. Natl. Acad. Sci. U.S.A.*, **109** (2012) 15691.
[186] Saam T., Herzen J., Hetterich H., Fill S., Willner M., Stockmar M., Achterhold K., Zanette I., Weitkamp T., Schüller U., Auweter S., Adam-Neumair S., Nikolau K., Reiser M. F., Pfeiffer F. and Bamberg F., *Plos One*, **8** (2013) e73513.
[187] Stampanoni M., Wang Z., Thüring T., David C., Roessl E., Trippel M., Kubik-Huch R. A., Singer G., Hohl M. K. and Hauser N., *Invest. Radiol.*, **46** (2011) 801.

[188] Zambelli J., Bevins N., Qi Z. and Chen G.-H., *Med. Phys.*, **37** (2010) 2473.
[189] Szafraniec M. B., Millard T. P., Ignatyev K., Speller R. D. and Olivo A., *Phys. Med. Biol.*, **59** (2014) N1.
[190] Hagen C. K., Endrizzi M., Diemoz P. C., Munro P. R. T. and Olivo A., *Med. Phys.*, **41** (2014) 070701.
[191] Makarova O. V., Mancini D. C., Moldovan N., Divan R., Tang C.-M., Ryding D. G. and Lee R. H., *Sensor. Actuat. A-Phys.*, **103** (2002) 182.
[192] Endrizzi M., Vittoria F. A., Diemoz P. C., Lorenzo R., Speller R. D., Wagner U. H., Rau C., Robinson I. K. and Olivo A., *Opt. Lett.*, **39** (2014) 3332.
[193] Diemoz P. C., Endrizzi M., Hagen C. K., Rau C., Bravin A., Speller R. D., Robinson I. K. and Olivo A., *JPCS*, **499** (2014) 012006.
[194] Olivo A., Hagen C. K., Millard T. P., Vittoria F., Diemoz P. C. and Endrizzi M., *Proc. SPIE*, **9033** (2014) 90330E.
[195] Roessl E., Daerr H., Koehler T., Martens G. and Van Stevendaal U., *Phil. Trans. R. Soc. A*, **372** (2014) 20130033.
[196] Ledermann W. and Lloyd E. (Editors), *Handbook of applicable mathematics-Volume VI: Statistics-Part A* (John Wiley & Sons) 1984.
[197] `http://vassarstats.net/textbook/index.html`.
[198] Statistical computation: October-December 2013, access to the site `http://vassarstats.net/tab2x2.html`.